

KAUNAS UNIVERSITY OF TECHNOLOGY

MANTAS SRIUBAS

**FORMATION AND INVESTIGATION OF SAMARIUM DOPED  
CERIUM OXIDE THIN FILMS**

Summary of Doctoral Dissertation,  
Technological Sciences, Materials Engineering (08T)

2018, Kaunas

This doctoral dissertation was prepared at Kaunas University of Technology, Faculty of Mathematics and Natural Sciences, Department of Physics during the period of 2013–2017. Part of the experiments was carried out at Lithuanian Energy Institute, Center for Hydrogen Energy Technologies. The studies were supported by Research Council of Lithuania.

**Scientific supervisor:**

Prof. Dr. Giedrius LAUKAITIS (Kaunas University of Technology, Physical Sciences, Physics – 02P)

**Editor:** Armandas Rumšas (Publishing Office “Technologija”)

**Dissertation Defence Board of Material Engineering Science Field:**

Prof. Dr. Habil. Arvidas GALDIKAS (Kaunas University of Technology, Physical Sciences, Physics – 02P) – **chairman**;

Prof. Dr. Diana ADLIENĖ (Kaunas University of Technology, Physical Sciences, Physics – 02P);

Prof. Dr. Habil. Maria GAZDA (Gdansk University of Technology, Technological Sciences, Material Engineering – 08T);

Dr. Viktoras GRIGALIŪNAS (Institute of Materials Science, Technological Sciences, Material Engineering – 08T);

Assoc. Prof. Dr. Tomas ŠALKUS (Vilnius University, Technological Sciences, Material Engineering – 08T).

The official defence of the dissertation will be held at 12 noon on 28<sup>th</sup> February, 2018 at the public meeting of Dissertation Defence Board of Material Engineering Science Field in Dissertation Defence Hall at Kaunas University of Technology.

Address: K. Donelaičio 73-403, LT-44249 Kaunas, Lithuania.

Tel. no. (+370) 37 300 042; fax. (+370) 37 324 144; e-mail [doktorantura@ktu.lt](mailto:doktorantura@ktu.lt).

Summary of doctoral dissertation was sent on 26<sup>th</sup> January, 2018.

The doctoral dissertation is available on the internet at <http://ktu.edu> and at the library of Kaunas University of Technology (K. Donelaičio 20, LT-44239 Kaunas, Lithuania).

KAUNO TECHNOLOGIJOS UNIVERSITETAS

MANTAS SRIUBAS

**SAMARIU LEGIRUOTO CERIO OKSIDO PLONŲJŲ  
SLUOKSNIŲ FORMAVIMAS IR TYRIMAS**

Daktaro disertacijos santrauka  
Technologijos mokslai, medžiagų inžinerija (08T)

2018, Kaunas

Disertacija rengta 2013–2017 metais Kauno technologijos universiteto Matematikos ir gamtos mokslų fakulteto Fizikos katedroje. Dalis mokslinių tyrimų buvo atlikta Lietuvos energetikos instituto Vandenilio energetikos technologijų centre. Mokslinius tyrimus rėmė Lietuvos mokslo taryba.

**Mokslinis vadovas:**

Prof. dr. Giedrius LAUKAITIS (Kauno technologijos universitetas, fiziniai mokslai, fizika – 02P)

**Redagavo:** Armandas Rumšas (leidykla „Technologija“)

**Medžiagų inžinerijos mokslo krypties disertacijos gynimo taryba:**

Prof. habil. dr. Arvidas GALDIKAS (Kauno technologijos universitetas, fiziniai mokslai, fizika – 02P) – **pirmininkas**;

Prof. dr. Diana ADLIENĖ (Kauno technologijos universitetas, fiziniai mokslai, fizika – 02P);

Prof. habil. dr. Maria GAZDA (Gdanskio technologijos universitetas, technologijos mokslai, medžiagų inžinerija – 08T);

dr. Viktoras GRIGALIŪNAS (Medžiagų mokslo institutas, technologijos mokslai, medžiagų inžinerija – 08T);

Prof. dr. Tomas ŠALKUS (Vilniaus universitetas, technologijos mokslai, medžiagų inžinerija – 08T).

Disertacija bus ginama viešame medžiagų inžinerijos mokslo krypties disertacijos gynimo tarybos posėdyje 2018 m. vasario 28 d. 12 val. Kauno technologijos universiteto disertacijų gynimo salėje.

Adresas: K. Donelaičio g. 73-403, 44249 Kaunas, Lietuva.

Tel. + 370 37 300 042; faks. + 370 37 324 144; el. paštas [doktorantura@ktu.lt](mailto:doktorantura@ktu.lt).

Disertacijos santrauka išsiųsta 2018 m. sausio 26 d.

Su disertacija galima susipažinti interneto svetainėje <http://ktu.edu> ir Kauno technologijos universiteto bibliotekoje (K. Donelaičio g. 20, 44239 Kaunas).

## CONTENTS

INTRODUCTION .....	6
1. EXPERIMENTAL TECHNIQUES .....	11
2. RESULTS .....	12
2.1. Influence of the Specific Surface Area of Ceramic Powders on the Selection of E-Beam Power .....	12
2.2. Evaluation of Elemental Composition and Its Influence on the Microstructure.....	13
2.3. Investigation of the Crystalline Structure of SDC Thin Films .....	15
2.4. Investigation of Surface Morphology of SDC Thin Films .....	23
2.5. Investigation of the Surface Roughness of SDC Thin Films.....	28
2.6. Evaluation of the Band Gap Energy of SDC Thin Films.....	32
2.7. Investigation of the Electrical Properties of SDC Thin Films .....	34
CONCLUSIONS.....	42
LIST OF REFERENCES .....	43
SANTRAUKA.....	50
CURRICULUM VITAE.....	51

## Introduction

Monitoring of  $O_2$ ,  $CO_x$ ,  $NO_x$  gas emissions, state of the art devices for oxygen, hydrogen and energy generation are of crucial importance in transport, steel, glass, paper, food industries and energetics[1-3]. The monitoring of  $O_2$ ,  $CO_x$ ,  $NO_x$  gas emissions is carried out by using gas sensors[4-9]. Hydrogen can be extracted from water by using electrolyzers whereas energy – by using solid oxide fuel cells[10, 11]. Oxygen ion conductors are employed in these devices.

$ZrO_2$ ,  $LaGaO_3$ ,  $CeO_2$ ,  $\delta$ - $Bi_2O_3$ ,  $Bi_4V_2O_{11}$ ,  $La_2Mo_2O_9$ ,  $LnBO_3$  (B=Al, In, Sc, Y) based ceramics and apatite ceramics are used for the manufacturing of oxygen ion conductors. However, not all materials are suitable because oxygen ion conductors must possess the following characteristics: high ionic conductivity, low electronic conductivity, stable crystalline structure across a wide range of temperatures and oxygen pressures, no chemical reactions with electrode materials, similar thermal expansion coefficient to electrode materials, low manufacturing cost, and adequate mechanical strength[12]. For example,  $La_{0.85}Sr_{0.15}Ga_{0.2}Mg_{0.2}O_{2.825}$  (LSGM) synthesis is complicated and expensive, although this type of ceramics exhibits high oxygen ion conductivity[13, 14].  $Bi_2O_3$  does not retain the stable phase across a wide range of temperatures[15, 16]. Even  $Y_{0.08}Zr_{0.92}O_2$  (8YSZ) is denoted by drawbacks, although it is still considered one of the best ionic conductors. The main drawback is its chemical reaction with  $La_{(1-x)}Sr_xMnO$  cathodes[17]. However, no chemical reactions between  $Sm_xCe_{1-x}O_{2-\delta}$  (SDC) ceramics and  $La_{(1-x)}Sr_xMnO$  cathodes have been observed. SDC also retains the stable phase up to the melting temperature, and its synthesis is much cheaper than LSGM. Moreover,  $Sm_{0.15}Ce_{0.85}O_{2-\delta}$  (0.018 S/cm) exhibits higher ionic conductivity than 8YSZ (0.0064 S/cm) at intermediate temperatures (600 °C)[13, 18-22]. However, oxygen diffuses to the surface of the electrolyte when the pressure of oxygen decreases and the temperature rises[23].  $Ce^{4+}$  reduction to  $Ce^{3+}$  occurs at the same time and SDC becomes an ionic-electronic conductor[24-27]. From the statements outlined above, it is possible to believe that SDC is the optimal choice at intermediate temperatures. The electrical properties of SDC depend on the Sm dopant concentration, the working temperature, the oxygen pressure, the migration path of oxygen ions, and the microstructure. It was established that  $CeO_2$  doped with 15 mol% Sm exhibits the highest ionic conductivity because the energy of vacancy activation is the lowest at this dopant concentration[19]. On the other hand, it is possible to change the electrical properties of ceramics by changing the crystallite size. The concentrations of vacancies are different in grains and grain boundaries. The concentration of oxygen vacancies decreases, and the concentration of electrons increases in the space charge zone near the grain interior[28-30]. Oxygen ion conductivity is higher in grains than in grain boundaries, and electron conductivity is higher in grain boundaries than in grains according to the Brick layer model[31]. Therefore,

ionic conductivity decreases with the decreasing grain size whereas electronic conductivity increases with the decreasing grain size because the ratio between the grain size ( $L$ ) and the grain boundary size ( $2b$ ) increases:  $2b/L$ [32].

Microstructural properties depend on the formation method and its parameters. Ionic conductors can be formed by using several different methods. One of them is the formation of ceramic pellets by pressing powder and heating pellets at a high temperature. The other method is the deposition of thin films on electrode materials. This method is superior because it enables us to deposit very thin films which are denoted by good adhesion, deposition consumes a lower amount of materials, and dopants distribute uniformly in thin films. Moreover, there are no impurities in thin films after deposition.

Thin films can be deposited by using the e-beam deposition method. This method has advantages in comparison with other methods, especially if materials with high melting temperatures are deposited. Materials can heat up to 3000–4000 °C temperatures. For this reason, it is possible to deposit ceramics, for example,  $CeO_2$  (considering its melting temperature of 2600 °C). In addition, it is possible to control the deposition rate between 0.02 nm/s and 10 nm/s and the grain size while using this method. Moreover, thin films are clean and uniform.

The main deposition parameters influencing the properties of the material are the deposition rate, the substrate temperature, the pressure and the specific surface area of powders. The influence of the substrate temperature and the deposition rate is more or less known. However, the influence of the specific surface area of powders on the properties of thin films is much less known. There are a few papers written by Virbukas where the influence of the specific surface area of powders is discussed. Virbukas studied  $Gd_{0.1}Ce_{0.9}O_{2-\delta}$  ( $S_{BET}$ : 6.44; 36.2; 201  $m^2/g$ ),  $Gd_{0.2}Ce_{0.8}O_{2-\delta}$  ( $S_{BET}$ : 5.8; 32.8; 220  $m^2/g$ ) and  $Sm_{0.15}Ce_{0.85}O_{2-\delta}$  ( $S_{BET}$ : 8; 39.3; 195  $m^2/g$ ) thin films which were deposited on room temperature substrates by using 0.2–1.6 nm/s deposition rate[33–35]. However, the influence of the specific surface area of powders on the properties of thin SDC films which were deposited onto higher temperature substrates was not investigated.

Therefore, it was decided to deposit  $Sm_{0.2}Ce_{0.8}O_{2-\delta}$  thin films by using powders of different specific surface areas: 6.2  $m^2/g$ , 11.3  $m^2/g$ , 38.8  $m^2/g$ , and 201.3  $m^2/g$ . Thin films were deposited on  $SiO_2$ , Alloy600, Si(100)  $Al_2O_3$  substrates whose temperatures were: 50 °C, 150 °C, 300 °C, 450 °C, 600 °C. In addition, thin films were deposited by using 0.2 nm/s, 0.4 nm/s, 0.8 nm/s, 1.2 nm/s and 1.6 nm/s deposition rates. The microstructure, the surface morphology and the electrical properties of thin films were investigated. X-ray diffraction, scanning electron microscopy, atomic force microscopy, energy-dispersive X-ray spectroscopy, X-ray photoelectron spectroscopy, electrochemical impedance spectroscopy, spectrophotometry and profilometry were used for the investigation.

## **The Main Objective**

To evaluate the influence of the specific surface area of powders, the deposition rate, the substrate temperature and the substrate type on the properties of  $\text{Sm}_{0.2}\text{Ce}_{0.8}\text{O}_{2-\delta}$  (SDC) thin films deposited by using the e-beam evaporation method.

The following tasks were carried out in order to achieve the main objective:

## **The Tasks of the Thesis**

1. To deposit SDC thin films on 50 °C, 150 °C, 300 °C, 450 °C, 600 °C temperature  $\text{SiO}_2$ , Alloy600, Si(100)  $\text{Al}_2\text{O}_3$  substrates by using powders of 6.2  $\text{m}^2/\text{g}$ , 11.3  $\text{m}^2/\text{g}$ , 38.8  $\text{m}^2/\text{g}$  and 201.3  $\text{m}^2/\text{g}$  specific surface area and 0.2 nm/s, 0.4 nm/s, 0.8 nm/s, 1.2 nm/s and 1.6 nm/s deposition rate.
2. To detect the dependences of the microstructure, surface morphology, electrical and optical properties on the specific surface area of the initial powder, the substrate temperature and the deposition rate.
3. To analyze and discuss the reasons and processes determining the dependences of the microstructure, the surface morphology, the electrical and optical properties on the deposition parameters.

## **Novelty of the Thesis**

1. It was determined that the e-beam power consumption required to achieve the same deposition rate is lower when using powders of a bigger specific surface area because atoms on the surface of particles have a lower binding energy than atoms inside the particles.
2. For the first time, the influence of the specific surface area of the initial powders was investigated on the microstructure of SDC thin films which were deposited on higher than the room temperature substrates, and it was determined that the preferential crystallographic orientation (111) changes to (200), (220) or (311) evaporating powder with 6.2  $\text{m}^2/\text{g}$  specific surface area, to (220) or (311) evaporating powders with 11.3  $\text{m}^2/\text{g}$  and 38.8  $\text{m}^2/\text{g}$  specific surface areas, and to (311) or (222) evaporating powder with 201.3  $\text{m}^2/\text{g}$  area if 450–600 °C substrate temperatures and/or 1.2–1.6 nm/s deposition rates are used.
3. For the first time, it was investigated and shown that the band gap of SDC thin films increases with the increasing crystallite size due to the decreased reduction rate of  $\text{Ce}^{4+}$  to  $\text{Ce}^{3+}$ .
4. The surface roughness of SDC thin films related to the growth kinetics of the crystallite size, i.e. the roughness of SDC thin films changes due to the different growth rates of crystallites in-plane and out-of-plane to the substrate.



### **Author's Contribution**

1. SDC thin films were deposited,
2. Microstructural morphological optical and electrical properties were investigated by using XRD, SEM, EDS, XPS, UV-VIS, AFM, and EIS methods.

### **Layout of the Thesis**

The length of the thesis is 166 pages. It contains 129 pictures, 30 tables and 238 references. The thesis consists of six parts: introduction, literature review, experimental techniques and methodology, results, conclusions and references.

### **Approbation**

The main results of this study have been published in 5 scientific articles; the results have also been presented in 7 scientific conferences.

### **Scientific Papers Related to the Topic of this Thesis:**

1. [D1] SRIUBAS, M., LAUKAITIS, G. (2015). *The influence of the Technological Parameters on the Ionic Conductivity of Samarium Doped Ceria Thin Films*. In: Material Science (Medžiagotyra), 2015. **21**(1).
2. [D2] SRIUBAS, M., PAMAKŠTYS, K. and LAUKAITIS, G. (2017). *Investigation of Microstructure and Electrical Properties of Sm Doped Ceria Thin Films*. In: Solid State Ionics, 2017. **302**: pp. 165–172.
3. [D3] VIRBUKAS, D., SRIUBAS, M. and LAUKAITIS, G. (2015). *Structural and Electrical Study of Samarium Doped Cerium Oxide Thin Films Prepared by E-Beam Evaporation*. In: Solid State Ionics, 2015. **271**: pp. 98–102.
4. [D4] SRIUBAS, M., BOČKUTĖ, K., VIRBUKAS, D., LAUKAITIS, G. (2015). *Dynamics of Electrical Charge Carriers in Mg-Doped TiO<sub>2</sub> Thin Films under Reducing Conditions*. In: Journal of Vibroengineering, 2015. **17**(6): pp. 2743–3391.
5. [D5] SRIUBAS, M. et al. (2014). *Investigation of the Properties of Ca-Doped TiO<sub>2</sub> Thin Films Formed by E-Beam Evaporation*. Procedia Engineering, 2014. **98**: pp. 133–138.

### **Other Scientific Papers**

1. SRIUBAS, M., LAUKAITIS, G. (2014). *The Properties of Calcium Doped Titanium Oxide Thin Films*. In: *Radiation Interaction with Materials: Fundamentals and Applications 2014: 5<sup>th</sup> International Conference, Kaunas, Lithuania, 2014: program and materials* / Kaunas University of Technology pp. 179–182.
2. SRIUBAS, M., LAUKAITIS, G. (2015). *Plonų Mg<sub>x</sub>Ti<sub>1-x</sub>O<sub>2</sub> sluoksnių, suformuotų garinant elektronų pluoštelį, savybių tyrimas // 41-oji Lietuvos nacionalinė fizikos konferencija, Vilnius: programa ir pranešimų tezės / Fizinių ir*

technologijos mokslų centras, Vilniaus universitetas, Kauno technologijos universitetas, Lietuvos fizikų draugija. ISBN 9786099551128.

3. SRIUBAS, M., LAUKAITIS, G. (2013). Technologinių parametru įtaka plonų samariu legiruotų cerio oksido sluoksnių savitajam joniniam laidžiui. In: *Medžiagų inžinerija '2013*. Kaunas, Lithuania.

#### **Conference Presentations:**

1. Sriubas, M., Laukaitis, G. (2013). Technologinių parametru įtaka plonų samariu legiruotų cerio oksido sluoksnių savitajam joniniam laidžiui. At: *Medžiagų inžinerija '2013*. Kaunas, Lithuania.

2. Sriubas, M., Laukaitis, G., Gajauskaitė, A., Bočkutė, K. (2014). The Properties of Calcium Doped Titanium Oxide Thin Films. At: *5<sup>th</sup> International Conference on Radiation Interaction with Materials: Fundamentals and Applications*. Kaunas, Lithuania.

3. Virbukas, D., Laukaitis, G., Sriubas, M. (2014). Structural and Electrical Study of Samarium Doped Cerium Oxide Thin Films Prepared by E-Beam Evaporation. At: *11<sup>th</sup> International Symposium on Systems with Fast Ionic Transport*. Gdansk, Poland.

4. Sriubas, M., Laukaitis, G. (2015). Plonų  $Mg_xTi_{1-x}O_2$  sluoksnių, suformuotų garinant elektronų pluošteliu, savybių tyrimas. At: *41<sup>st</sup> National Physics Conference of Lithuania*.

5. Sriubas, M., Laukaitis, G. (2015). Mg and Ca Doping Influence on the Microstructure and the Properties of  $TiO_2$  Thin Films. At: *2015 Inter-Academia, September 28–30, 2015*. Hamamatsu, Japan.

6. Sriubas, M., Laukaitis, G., Bočkutė, K., Pamakštys, K., Kainbaev, N., Ramanauskas, M. (2016). Investigation of Microstructure and Electrical Properties of Sm Doped Ceria Thin Films. At: *12<sup>th</sup> International Symposium on Systems with Fast Ionic Transport*. July 03, 2016. Kaunas, Lithuania.

7. Sriubas, M., Kainbaev, N., Laukaitis, G. (2016). Influence of Substrate Temperature, Deposition Rate, and Evaporating Material Properties on Microstructure and Surface Morphology of SDC Thin Films Deposited by E-Beam Technique. At: *2016 Inter-Academia*. September 26–28, 2016. Warsaw, Poland.

## 1. Experimental Techniques

Sm doped cerium oxide thin films were deposited on SiO<sub>2</sub>, Si(100), Alloy 600 (Fe-Ni-Cr), and Al<sub>2</sub>O<sub>3</sub> substrates. The substrates were ultrasonically cleaned in pure acetone for 10 min. Thin films were formed with e-beam physical vapour deposition system *Kurt J. Lesker EB-PVD 75* by using 0.2 nm/s±1.6 nm/s deposition rate, substrate temperatures from 50 °C to 600 °C, and 5·10<sup>-7</sup> bar working pressure. The Sm<sub>0.2</sub>Ce<sub>0.8</sub>O<sub>2-δ</sub> powder (*Nexceris*, LLC, Fuelcellmaterials, USA) of 6.2 m<sup>2</sup>/g, 11.3 m<sup>2</sup>/g, 38.8 m<sup>2</sup>/g, 201.3 m<sup>2</sup>/g surface area was used as the evaporating material. It was pressed into pellets by using a mechanical press (303.5 MPa pressure). The pellets were placed into a crucible, and a vacuum chamber was depressurized up to 2·10<sup>-9</sup> bar. After that, the substrates were treated with Ar<sup>+</sup> ion plasma (10 min) and preheated up to the working temperature. The thickness and THE deposition rate were controlled with an *INFICON crystal sensor*. The structure of the deposited thin films was investigated by using an X-ray diffractometer (XRD) *Bruker D8 Discover* at 2Θ angle within a range of 20°–70° while using Cu Kα (λ=0.154059 nm) radiation, 0.01° step, and a *Lynx eye* PSD detector. *EVA Search – Match* software and a *PDF-2* database were used to identify the diffraction peaks. *TOPAS* software was used for crystallite size calculations. Measured patterns were fitted by using Pawley's method. The crystallite size was calculated by using Scherrer's equation[36]:

$$\langle d \rangle = \frac{K \lambda_R}{\beta \cos\theta}, \quad (1.1)$$

where  $\langle d \rangle$  is the crystallite size of the material,  $\lambda_R$  is the wavelength of the X-ray radiation,  $\beta$  is the full width at half maximum,  $K$  is the correction factor, and  $\theta$  is the angle of diffraction.

Texture coefficient  $T_{(hkl)}$  was determined by using formula[37]:

$$T_{(hkl)} = \frac{I(hkl)}{I_0(hkl)} \left[ \frac{1}{n} \sum_1^n \frac{I(hkl)}{I_0(hkl)} \right]^{-1}, \quad (1.2)$$

where  $I(hkl)$  is the intensity of the XRD peak corresponding to  $(hkl)$  planes,  $n$  is the number of the diffraction peaks taken into account,  $I_0(hkl)$  denotes the intensity of the XRD peak in the *EVA Search – Match* software database.  $T_{(hkl)} = 1$  corresponds to films with randomly oriented crystallites, while higher values indicate the large number of grains oriented in a given  $(hkl)$  direction. The surface topography images and the cross-section images were obtained with a scanning electron microscope *Hitachi S-3400N* (SEM). The surface roughness measurements of SDC thin films were carried out with an atomic force microscope *AFM NT-206* while using the dynamic mode during measurements. The obtained data was processed by using the *Surface Explorer* software. The elemental composition was controlled by using an energy-dispersive X-ray spectroscopy *BrukerXFlash QUAD 5040* (EDS). Ce<sup>3+</sup> and Ce<sup>4+</sup> concentrations were determined

by the XPS method (PHI 5000 Versaprobe). The measurements were conducted by using monochromatic X-ray radiation ( $AlK_{\alpha}$ , 1486.6 eV). The X-ray beam power was 23.2 W, the diameter of the beam was 100 mm, and the measurement angle was  $45^{\circ}$  during the experiments. Thin films were not sputtered before measurements in order to avoid changes of the thin SDC film surface structure. The sample charging effect was compensated by using radiation of low energy electrons and ions. The experimental data was curve-fitted by using Gaussian-Lorentzian functions, and the background was eliminated by using the Shirley method. *MultiPak* software was used for curve fitting. The concentrations of  $Ce^{3+}$  were calculated by using these spectra and the following equation:

$$C_{Ce^{3+}} = \frac{A_{V_0} + A_{U_0} + A_{V'} + A_{U'}}{A_{V'} + A_{U'} + A_{V''} + A_{U''} + A_{V'''} + A_{U'''} + A_{V_0} + A_{U_0} + A_{V'} + A_{U'}} \quad (1.3)$$

where  $C_{Ce^{3+}}$  is  $Ce^{3+}$  concentration,  $A$  – the areas of particular peaks ( $V_0$  –  $Ce^{3+}3d_{5/2}$ ,  $V$  –  $Ce^{4+}3d_{5/2}$ ,  $V'$  –  $Ce^{3+}3d_{5/2}$ ,  $V''$  –  $Ce^{4+}3d_{5/2}$ ,  $V'''$  –  $Ce^{4+}3d_{5/2}$ ,  $U_0$  –  $Ce^{3+}3d_{3/2}$ ,  $U$  –  $Ce^{4+}3d_{3/2}$ ,  $U'$  –  $Ce^{3+}3d_{3/2}$ ,  $U''$  –  $Ce^{4+}3d_{3/2}$ ,  $U'''$  –  $Ce^{4+}3d_{3/2}$ ).

Optical transmittance spectra were measured by using a *UV-VIS 650* spectrometer. The band gap calculations were carried out by using the Tauc relation:

$$(h\nu_f \alpha)^{\frac{1}{n}} = A(h\nu - E_g) \quad (1.4)$$

where  $h$  is the Plank constant,  $\nu_f$  denotes the photon frequency,  $\alpha$  is the absorption coefficient,  $E_g$  represents the band gap,  $A$  denotes the proportionality constant, and  $n$  stands for 1/2, 3/2, 2 or 3.

The total conductivity was investigated by using *NorECsAS* (EIS), an impedance spectrometer. The total conductivity was measured only for thin films deposited on  $Al_2O_3$  in order to avoid the influence of the substrate on the measurements. The Pt electrodes were applied on the top of thin films by using a mask reproducing the geometry of the electrodes. The distance between the Pt electrodes was 10 mm, and their dimensions were 3 mm  $\times$  10 mm. The measurements were carried out in  $1 \div 10^6$  Hz frequency range and in the 200  $^{\circ}C \div 1000$   $^{\circ}C$  temperature interval by using the two-probe method.

## 2. Results

### 2.1. Influence of the Specific Surface Area of Ceramic Powders on the Selection of E-Beam Power

It was observed that the deposition rate of SDC thin films depends on the e-beam power whereas the e-beam power required to maintain the same deposition rate depends on the specific surface area of powders  $S_{BET}$ , see **Fig. 2.1**. The dependence of the deposition rate on the e-beam power is exponential. The kinetic

energy of electrons increases with the increasing e-beam power. So, the more the kinetic energy of electrons is transferred to phonon excitation, the more the temperature of the material increases as well. It means that the saturated vapor pressure and the vapor flux increase while increasing the temperature of the material[38].

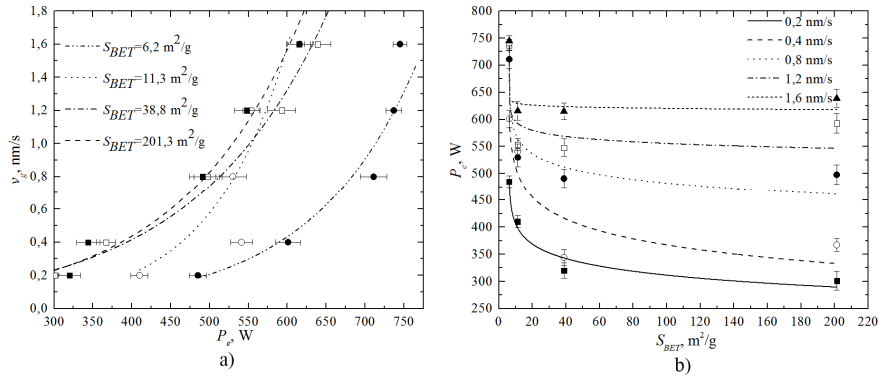


**Fig. 2.1** a) Influence of the e-beam power ( $P_e$ ) on the deposition rate ( $v_g$ ) and b) on the required power of the e-beam to maintain the fixed deposition rate evaporating powders of different specific surface areas ( $S_{BET}$ )

A more important phenomenon is that the e-beam power required to maintain the same deposition rate is lower while using the powders of a bigger specific surface area for evaporation, see **Fig. 2.1, b**. For example, in order to achieve a deposition rate of 0.2 nm/s, the power of 485 W is required when using the powder of a specific surface area of 6.2 m<sup>2</sup>/g, and 301 W when using the powder of a specific surface area of 201.3 m<sup>2</sup>/g.

The ratio of the surface area to the volume increases with the increasing specific surface area of powder particles. Moreover, the atoms which are on the surface of a particle have a lower number of neighbors than the atoms inside a particle. Hence the atoms which are on the surface of a particle have a weaker binding energy than the atoms which are inside a particle. Thus the melting temperature decreases with the increasing specific surface area of the powder. Therefore, the e-beam power required to maintain the same deposition rate is lower when using powders of a bigger specific surface area[39, 40]. A composition of the vapor phase depends on the specific surface area as well, i.e., vapors can consist of different numbers of atomic particles and atomic clusters[41].

## 2.2. Evaluation of Elemental Composition and Its Influence on the Microstructure

It has been found that the Sm concentration varies significantly from 5.7 mol% to 21.0 mol% in SDC thin films. However, a vast majority of SDC thin films

contain about 11–12 mol% samarium, which is a lot less than in the initial powders (~20 mol%). Such a difference of concentrations is influenced by the evaporation mechanism. It is known that  $\text{CeO}_2$  and  $\text{Sm}_2\text{O}_3$  change their phase from solid to gaseous during the sublimation process[42]. The sublimation of  $\text{CeO}_2$  starts at a temperature of 1950 °C whereas the sublimation of  $\text{Sm}_2\text{O}_3$  commences at a temperature of 2100 °C[43]. The difference between the two sublimation temperatures is 150 °C. It means that the sublimation rates at the same temperature should be different. The ratio of Sm atoms to Ce atoms in the vapor phase is smaller than in the initial powder. Hence the Sm concentration in SDC thin films is lower than in the initial powder.

The reasons of the variation of the Sm concentration are not known. However, 21 mol% of samarium does not exceed the solubility limit (~45%) in  $\text{CeO}_2$ [44]. For this reason, the dopants do not influence the microstructure or the surface morphology of SDC thin films. The plot of the crystallite size dependence on the dopant concentration confirms it, as it is evidently shown in **Fig. 2.2, a**.

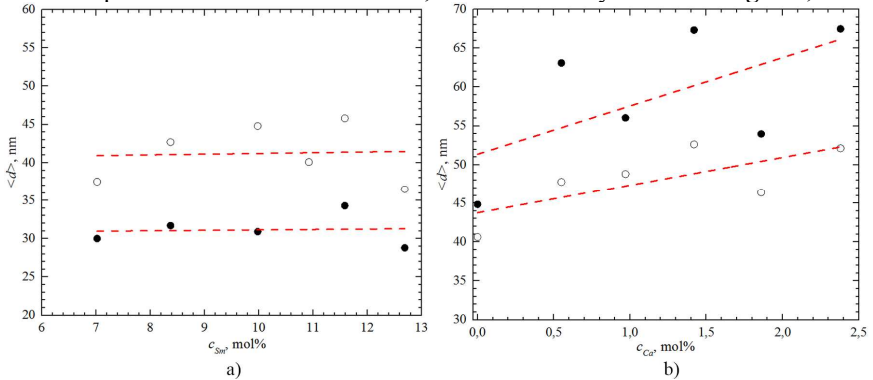


**Fig. 2.2** Crystallite size dependence on the dopant concentration: a) SDC thin films and b)  $\text{TiO}_2$  doped  $\text{Ca}^{[\text{D4}, \text{D5}]}$

The crystallite size is almost the same with the increasing Sm concentration. It is about 30 nm when using  $\text{SiO}_2$  substrates and about 41 nm when using Alloy 600 substrates. In comparison, the crystallite size depends on the dopant concentration in Ca-doped  $\text{TiO}_2$ , see **Fig. 2.2, b**<sup>[D4, D5]</sup>. The reason for the crystallite size increase is that the crystallite size depends on the dopant concentration if it exceeds the solubility limit[45, 46]. The solubility limit for Ca in  $\text{TiO}_2$  is under discussion, but it is not expected to be higher than 2%[47, 48].

It has been calculated that the oxygen concentration (70.2–72.5 mol%) is higher at the level of 4 mol% to 5 mol% than the stoichiometric concentration (66.6 mol%). However, it is known that ceria is a nonstoichiometric oxide which is denoted by oxygen deficit ( $\text{CeO}_{2-\delta}$ ). The explanation of the oxygen excess is the following. Oxygen desorption from  $\text{CeO}_2$  takes place when the temperature

increases and the pressure decreases[49]. In addition, oxygen desorption occurs from the pores of pressed pellets. The vapor phase consists of CeO, O<sub>2</sub>, and Sm particles. It means that oxygen condenses on the surface of the substrate and diffuses into it. Also, oxygen can diffuse from SDC thin film into the substrate[50, 51]. A thin oxide layer forms on the substrate due to oxygen diffusion. EDS measurement is based on the measurement of characteristic X-rays. The depth from which an EDS detector registers the characteristic X-rays can reach several micrometers. Therefore, the signal recorded during the measurement consists of the SDC thin film, oxide layer and substrate components.

### 2.3. Investigation of the Crystalline Structure of SDC Thin Films

SDC thin films feature peaks belonging to (111), (200), (220), (311), (222), and (400) crystallographic orientations. The positions of the peaks correspond to the fluorite structure, the Fm3m space group. However, SDC thin films do not necessarily possess all of these peaks. Peaks can disappear, or their intensities can increase by changing the deposition parameters.

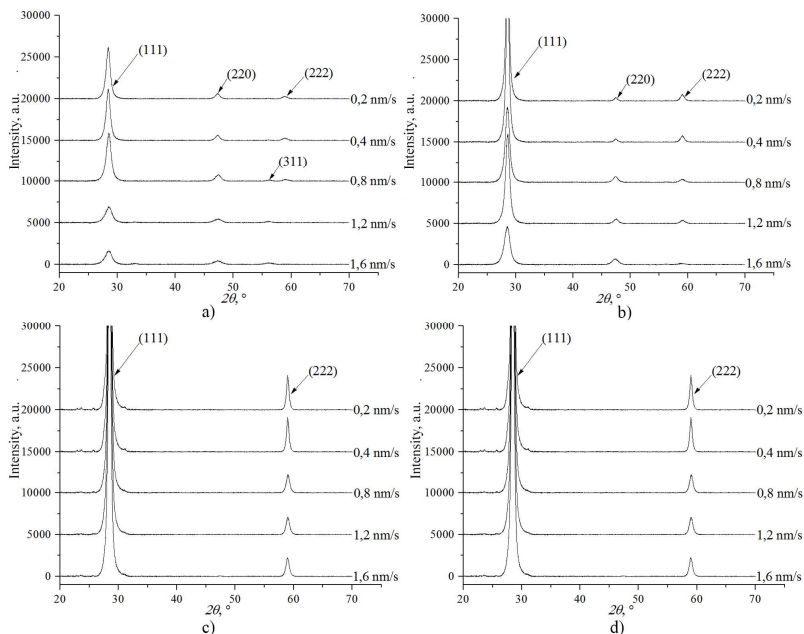


**Fig. 2.3** XRD patterns of SDC thin films deposited by using powder of  $S_{BET}=11.3 \text{ m}^2/\text{g}$  and a different temperature of SiO<sub>2</sub> substrate: a) 50 °C, b) 150 °C, c) 300 °C and d) 450 °C

SDC thin films deposited on 50 °C temperature substrates have 4 peaks corresponding to (111), (220), (311), and (222) crystallographic orientations. Thin

films deposited on 150 °C temperature substrates have 3 peaks corresponding to (111), (220), and (222) crystallographic orientations, whereas SDC thin films deposited on 300 °C and 450 °C temperature substrates have only 2 peaks corresponding to (111) and (222) orientations, see **Fig. 2.3**. In addition, the intensity of the peaks increases when using substrates of a higher temperature and decreases when using a higher deposition rate. The results are very similar to the results obtained in the experiments conducted by M.S. Anwar and R. Narasimha [52, 53].

The crystalline structure of  $\text{Sm}_{0.15}\text{Ce}_{0.85}\text{O}_{2-\delta}$  (SDC 15) thin films deposited by evaporating SDC 15 powder repeats the crystalline structure of the initial powder, see **Fig. 2.4**<sup>[D3]</sup>. Moreover, thin films have similar peaks to those of  $\text{Sm}_{0.2}\text{Ce}_{0.8}\text{O}_{2-\delta}$ .

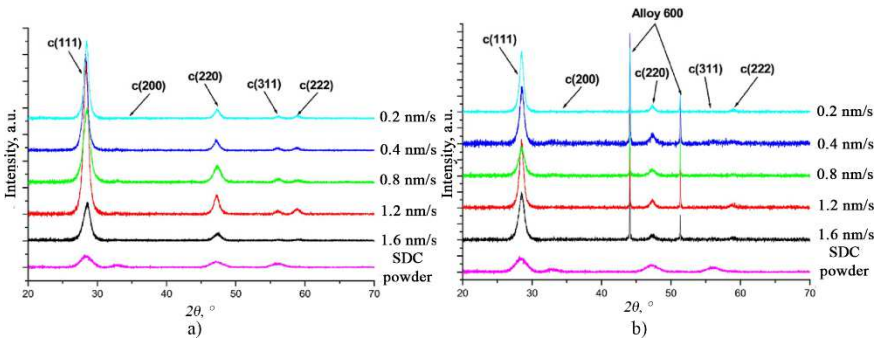


**Fig. 2.4** XRD patterns of SDC thin films deposited by using powder of  $S_{BET}=195 \text{ m}^2/\text{g}$  and 50 °C temperature substrates: a)  $\text{SiO}_2$  and b) Alloy 600<sup>[D3]</sup>

All the SDC thin films deposited on 50 °C, 150 °C, and 300 °C temperature substrates have a similar structure, see **Fig. 2.3**. No influence of the substrate type, the specific area of powder or the concentration of the initial powder was observed. A different situation develops when using 450 °C temperature substrates. Exception is  $\text{SiO}_2$  substrates, the deposition parameters did not influence the microstructure when using 450 °C temperature substrates **Fig. 2.3, d**. When using other substrates, the influence of the substrate temperature, the substrate type, the deposition rate, and the specific surface area of the powders on the crystalline structure of SDC thin films was observed, see **Fig. 2.5, Fig. 2.6, Fig. 2.7**.

SDC thin films deposited while evaporating powders of different surface areas on  $\text{SiO}_2$  substrates (600 °C) have different crystalline structures, see **Fig. 2.5**. X-ray diffraction patterns of SDC thin films deposited when evaporating  $6.2 \text{ m}^2/\text{g}$  powder exhibit peaks corresponding to (111), (200), (220), (311), (222), and (400) crystallographic orientations<sup>[D2]</sup>. X-ray diffraction patterns of SDC thin films deposited when evaporating  $38.8 \text{ m}^2/\text{g}$  powder feature peaks corresponding to (111), (200), (220), (311), and (222) crystallographic orientations<sup>[D1]</sup>. (400)



orientation peak disappears, (200) and (222) orientation peaks sharply decrease, and more X-ray diffraction spectra with a lower intensity of (220) and (311) orientation peaks appear in X-ray diffraction patterns. X-ray diffraction patterns of SDC thin films deposited when evaporating 11.3 m<sup>2</sup>/g powder show peaks corresponding to (111), (220), (311), and (222) crystallographic orientations. In this case, (200) crystallographic orientation disappears. An arrangement of diffraction peaks in SDC thin films deposited when evaporating powder of 201.3 m<sup>2</sup>/g specific surface area is very similar to the arrangement in SDC thin films deposited when evaporating powder of 11.3 m<sup>2</sup>/g specific surface area, see **Fig. 2.5**.

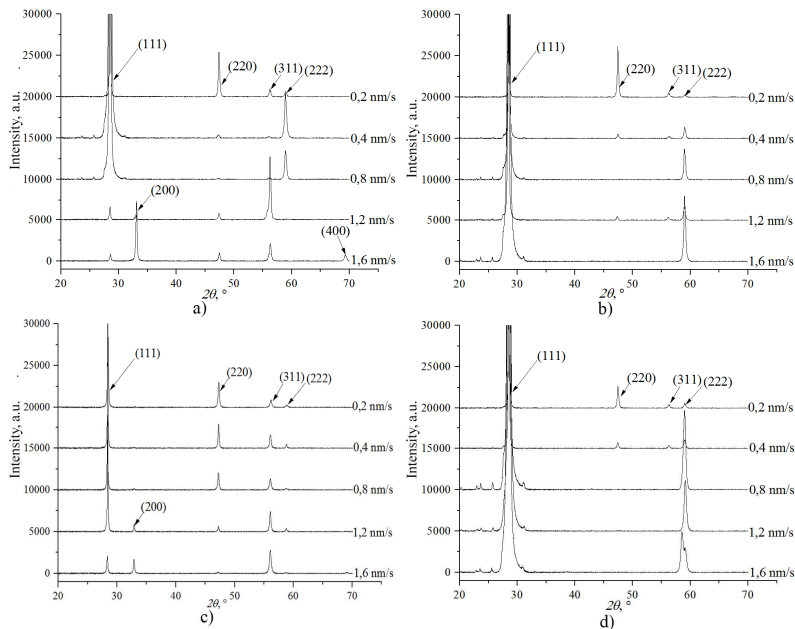


**Fig. 2.5** XRD patterns of SDC thin films deposited on 600 °C temperature SiO<sub>2</sub> substrates when using powders of different specific surface areas: a)  $S_{BET}=6.2$  m<sup>2</sup>/g<sup>[D2]</sup>, b)  $S_{BET}=11.3$  m<sup>2</sup>/g, c)  $S_{BET}=38.82$  m<sup>2</sup>/g<sup>[D1]</sup> and d)  $S_{BET}=201.3$  m<sup>2</sup>/g

It is possible to conclude that the peaks of (111) and (222) crystallographic orientations increase whereas the peaks of (200), (220), (311) and (400) crystallographic orientations disappear or decrease with the increasing specific surface area of the powders. In addition, the peaks of (220) crystallographic orientations increase when using 0.2 nm/s deposition rate whereas the peaks of (200) and (311) crystallographic orientations increase when using 1.2 nm/s–1.6 nm/s deposition rates. An exception is SDC thin films deposited when evaporating powder of 38.8 m<sup>2</sup>/g specific surface area. The obtained results are similar to the results received in the experiments conducted by Mansilla[54].

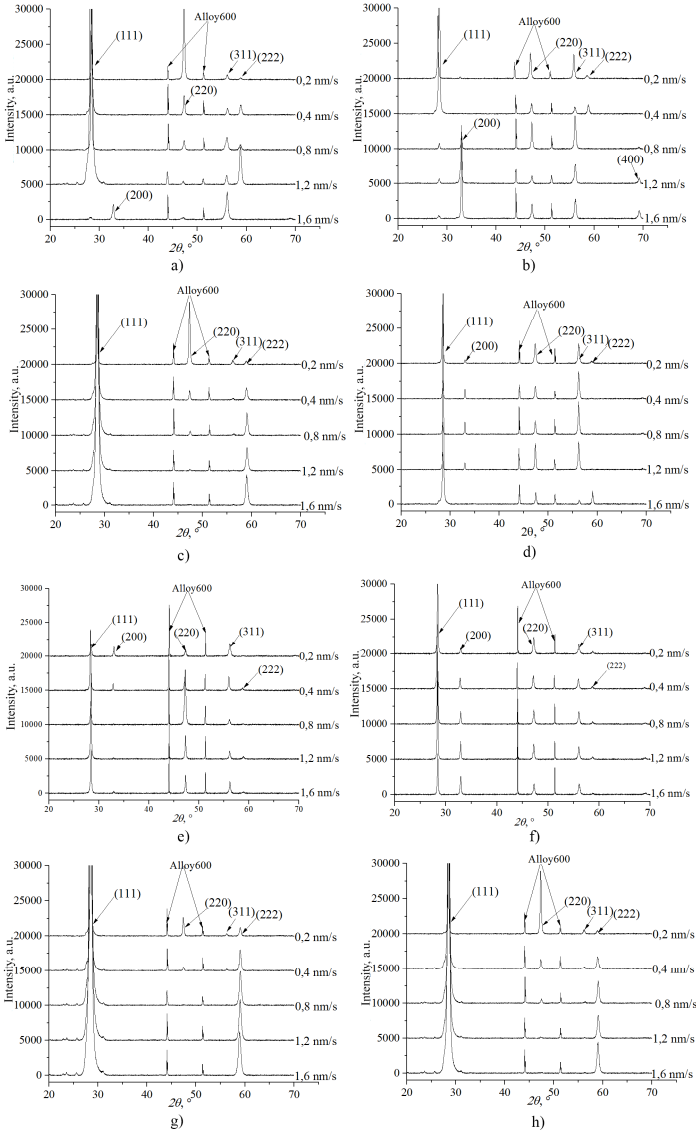


**Fig. 2.6** XRD patterns of SDC thin films deposited on Alloy600 substrates when using powders of different specific surface areas: a)  $S_{\text{BET}}=6.2 \text{ m}^2/\text{g}$ ,  $450 \text{ }^\circ\text{C}^{[\text{D}2]}$ , b)  $S_{\text{BET}}=6.2 \text{ m}^2/\text{g}$ ,  $600 \text{ }^\circ\text{C}^{[\text{D}2]}$ , c)  $S_{\text{BET}}=11.3 \text{ m}^2/\text{g}$ ,  $450 \text{ }^\circ\text{C}$ , d)  $S_{\text{BET}}=11.3 \text{ m}^2/\text{g}$ ,  $600 \text{ }^\circ\text{C}$ , e)  $S_{\text{BET}}=38.82 \text{ m}^2/\text{g}$ ,  $450 \text{ }^\circ\text{C}^{[\text{D}1]}$ , f)  $S_{\text{BET}}=38.82 \text{ m}^2/\text{g}$ ,  $600 \text{ }^\circ\text{C}^{[\text{D}1]}$ , g)  $S_{\text{BET}}=201.3 \text{ m}^2/\text{g}$   $450 \text{ }^\circ\text{C}$ , h)  $S_{\text{BET}}=201.3 \text{ m}^2/\text{g}$   $600 \text{ }^\circ\text{C}$

The crystallographic structure of SDC thin films formed on Alloy 600 substrates as shown in **Fig. 2.6** is slightly different from the case above. The peaks of (200) crystallographic orientation appear when evaporating powders of 6.2 m<sup>2</sup>/g and 38.8 m<sup>2</sup>/g specific surface area when the temperature of the substrate is 450 °C, and the deposition rates are 0.2 nm/s, 0.4 nm/s and 1.6 nm/s. There are more X-ray patterns with the peak of (200) crystallographic orientation evaporating powders of 6.2 m<sup>2</sup>/g, 11.3 m<sup>2</sup>/g, and 38.8 m<sup>2</sup>/g specific surface area when the substrate temperature is 600 °C<sup>[D1,D2]</sup>. The peaks are visible when using almost all the deposition rates. The peak intensity of (220) and (311) crystallographic orientations decreases with the increasing specific surface area of powders and the increasing deposition rate. The peaks intensities of (111) and (222) crystallographic orientations increase with the increasing specific surface area of evaporating powders.

The crystallographic structure of SDC thin films deposited on Si(100) substrates as shown in **Fig. 2.7** is similar to the crystallographic structure of SDC thin films deposited on SiO<sub>2</sub> substrates. The peak of (200) crystallographic orientation is visible when evaporating the powder of 6.2 m<sup>2</sup>/g specific surface area and using 1.6 nm/s deposition rate if the temperature of the substrates is 450 °C; also, if the temperature of the substrates is 600 °C, the peak of (200) crystallographic orientation is visible when using 1.2 nm/s–1.6 nm/s deposition rate or 0.2 nm/s–0.4 nm/s deposition rate and the powders of 6.2 m<sup>2</sup>/g and 11.3 m<sup>2</sup>/g specific surface area, respectively. The intensities or existence of the peaks of (220) and (311) crystallographic orientations depend on the specific surface area of evaporating powders and on the deposition rate. The intensities of the peaks of (220) and (311) crystallographic orientations decrease while increasing both deposition parameters and vice versa for the peaks of (111) and (222) crystallographic orientations.

A more accurate analysis of the crystallographic structure is obtained after the calculations of the texture coefficient. The data shows that the preferred crystallographic orientation (111) (green data points) changes only at a high temperature (450 °C–600 °C) and high deposition rates (1.2 nm/s–1.6 nm/s). The preferred crystallographic orientation (111) changes to (200), (220), (311) or (222). The preferred crystallographic orientation (111) changes to (200), (220) and (311) when using the powder of 6.2 m<sup>2</sup>/g specific surface area. For example, preferred orientation (111) changes to (200) ( $T_{111} = 0.1$ ;  $T_{200} = 3.0$ ) if SDC thin films are deposited on 600 °C temperature SiO<sub>2</sub> substrates while using the 1.6 nm/s deposition rate. Preferred crystallographic orientation (111) changes to (220) or (311) when using the powders of 11.3 m<sup>2</sup>/g and 38.8 m<sup>2</sup>/g specific surface area. For example, preferred orientation (111) changes to (311) ( $T_{111} = 0.4$ ;  $T_{311} = 1.9$ ) if SDC thin films are deposited while evaporating the powder of 11.3 m<sup>2</sup>/g specific surface area on 600 °C temperature Alloy600 substrates when using the 1.2 nm/s deposition rate. Preferred crystallographic orientation (111) changes to (311) or (222) when using the powder of 201.3 m<sup>2</sup>/g specific surface area. For example, preferred orientation (111) changes to (311) ( $T_{111} = 1.2$ ;  $T_{311} = 1.6$ ) if SDC thin films are deposited on 150 °C temperature Alloy600 substrates when

using the 1.6 nm/s deposition rate. Moreover, a lower number of thin films change the preferred orientation with the increasing specific surface area of the powders. The substrate type also exerts influence on the crystallographic structure. The highest number of SDC thin films change their preferred orientation if they are deposited on Alloy600 substrates whereas the lowest number of SDC thin films change their preferred orientation if they are deposited on SiO<sub>2</sub> substrates while the influence of Si(100) substrates is in the middle.

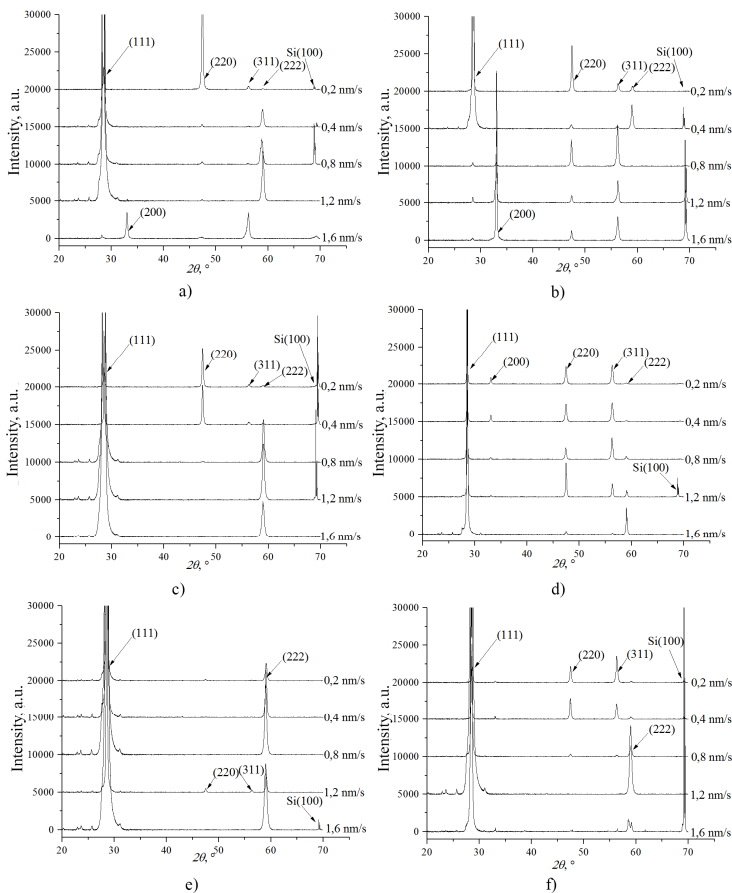


**Fig. 2.7** XRD patterns of SDC thin films deposited on Si(100) substrates when using powders of different specific surface area: a)  $S_{BET}=6.2 \text{ m}^2/\text{g}$ , 450 °C, b)  $S_{BET}=6.2 \text{ m}^2/\text{g}$ , 600 °C, c)  $S_{BET}=11.3 \text{ m}^2/\text{g}$ , 450 °C, d)  $S_{BET}=11.3 \text{ m}^2/\text{g}$ , 600 °C, e)  $S_{BET}=201.3 \text{ m}^2/\text{g}$ , 450 °C, f)  $S_{BET}=201.3 \text{ m}^2/\text{g}$ , 600 °C

The crystalline structure of SDC thin films depends on the composition of the vapor phase during the evaporation process. It is known that ceria changes its phase from solid to gas during partial dissociation in the condensed phase  $(CeO_2)_K \rightarrow (xCe)_G + (yO_2)_G + (zCeO)_G$ . In other words, the vapor consists of  $CeO_2$ , CeO, Ce and  $O_2$ . In the case of SDC, Sm is changed part of Ce. Therefore, vapor of SDC consists of Sm,  $CeO_2$ , CeO, Ce and  $O_2$ . The ratio of atoms to compounds in the vapor flux depends on the ratio of Ce to  $CeO_2$  on the surface of the evaporating powder. The vapor phase consists of  $CeO_2$ , CeO, and Ce where the concentrations of CeO and Ce are lower than the concentration of  $CeO_2$  from 4 to 6 times, respectively, if bulk  $CeO_2$  evaporates. However, the vapor phase consists of  $CeO_2$ , CeO, and Ce, whereas the concentrations of  $CeO_2$  and Ce are lower than the concentration of CeO from 5 to 100 times, respectively, if the mixture of Ce– $CeO_2$  evaporates[55]. Moreover, reduction of  $CeO_2$  occurs on the surface (~7 nm) of  $CeO_2$ [26, 27]. It means that a larger surface area of SDC powder is reduced if the evaporation powder of a larger specific surface area is used, i.e., deficit of oxygen will be observed. Experiments conducted by Orliukas prove this statement. The researcher discovered that  $Ce^{3+}$  concentration equals 14.16% when using powders of 8 m<sup>2</sup>/g specific surface area and reaches 19.47 % when using the powders of 203 m<sup>2</sup>/g specific surface area[56]. Therefore, there is more CeO, Ce, and Sm and less  $CeO_2$  in the vapor phase when powders of a larger specific surface area are used.

Molecule dissociation or diffusion occurs after a molecule has reached the substrate surface. However, the dissociation time of  $CeO_2$  is longer while the diffusion distance and time for  $CeO_2$  are shorter than for CeO or adatoms.

It means that the probability to form a crystallographic plane of a higher surface energy ( $\gamma_{(111)} < \gamma_{(200)} < \gamma_{(220)} < \gamma_{(311)}$ ) is higher when the concentration of  $CeO_2$  is higher in the vapor flux. A similar effect is observed when using a higher deposition rate. Adatoms do not have enough time to occupy the lowest energy state.

The diffusion distance increases for adatoms and molecules when using substrates of a higher temperature. Thus more surfaces of low surface energy ((111) and (222)) are formed. Possibly, the probability to form surfaces of (111) and (222) strongly decreases due to the prominent decrease of the surface energy at high temperatures. In this case, more surfaces of a higher surface energy form, i.e. (200), (220), (311) or (400) are obtained. It means that the probability of changing the preferred orientation increases.

The influence of the substrate on the crystalline structure is related to surface oxidation. EDS measurements revealed that the concentration of oxygen is higher in SDC thin films than the stoichiometric concentration. Moreover, EDS signal recorded during the measurement consists of the SDC thin film, the oxide layer and the substrate components. It means that the oxide layer is formed on the surface of the substrate. The oxidation rate is different on different substrates.

Probably, Alloy600 is less active than Si(100). Consequently, the influence of Alloy600 substrate on the crystalline structure is stronger than Si(100).

The crystallite size calculations revealed that the crystallite size is higher when using substrates of a higher temperature, see **Fig. 2.8**. However, the crystallite size not necessarily is higher at higher temperatures (450 °C–600 °C). Such a deviation from the dependence is due to the changes in the preferred crystallographic orientation and because of the number of additional planes ((200), (220), (311), (400)). The crystallite size decreases when the preferred orientation changes. The crystallite size also decreases when SDC thin films have a high number of additional crystallographic planes. The diffusion rate of adatoms is higher and the distance is longer when using substrates of a higher temperature. In this situation, larger crystallites form. However, the diffusion length is shorter on the surface with a higher surface energy ( $\gamma_{(111)} < \gamma_{(200)} < \gamma_{(220)} < \gamma_{(311)}$ ). Therefore, crystallites grow smaller on surfaces with a higher energy.

The growth rate also exerts influence on the crystallite size. Crystallites are formed smaller when using a higher deposition rate. In comparison, it is possible to analyze SDC thin films deposited on 450 °C temperature SiO<sub>2</sub> substrates when using the 0.2 nm/s–1.6 nm/s growth rate. The crystallite size changes from 80.6 nm to 48.0 nm when using the powder of 6.2 m<sup>2</sup>/g specific surface area<sup>[D2]</sup>. The crystallite size changes from 48.9 nm to 28.6 nm when using the powder of 11.3 m<sup>2</sup>/g specific surface area. The crystallite size changes from 49.5 nm to 35.0 nm when using the powder of 38.8 m<sup>2</sup>/g specific surface area<sup>[D1]</sup>. The crystallite size changes from 39.2 nm to 26.5 nm when using the powder of 201.3 m<sup>2</sup>/g specific surface area. A higher number of nucleation centers are formed while using a higher deposition rate. What is more, a high number of nucleation centers limit the growth of crystallites.

The influence of a specific surface area of powders on the crystallite size was observed only for SDC thin films deposited at high temperatures (450 °C–600 °C). The crystallite size changes from 6.8 nm (50 °C) to 66.5 nm (600 °C) in SDC thin films deposited by evaporating powder of 6.2 m<sup>2</sup>/g specific surface area on SiO<sub>2</sub> substrates<sup>[D2]</sup>. The crystallite size changes from 6.4 nm (50 °C) to 89.1 nm (600 °C) in SDC thin films deposited by evaporating powder of 11.3 m<sup>2</sup>/g specific surface area on SiO<sub>2</sub> substrates. The crystallite size changes from 10.4 nm (50 °C) to 97.3 nm (600 °C) in SDC thin films deposited by evaporating the powder of 38.8 m<sup>2</sup>/g specific surface area on SiO<sub>2</sub> substrates<sup>[D1]</sup>. The crystallite size changes from 5.4 nm (50 °C) to 91.8 nm (600 °C) in SDC thin films deposited by evaporating the powder of 201.3 m<sup>2</sup>/g specific surface area on SiO<sub>2</sub> substrates. Such changes in the crystallite size prove the statement that CeO and Ce concentrations are higher when using powders of a higher specific surface area. The diffusion rates of CeO dissociation products and Ce adatoms are higher than the diffusion rates of CeO<sub>2</sub> molecules or their dissociation products on the surface

of the substrate. For this reason, the crystallite size should be larger when using powders of a larger specific surface area.

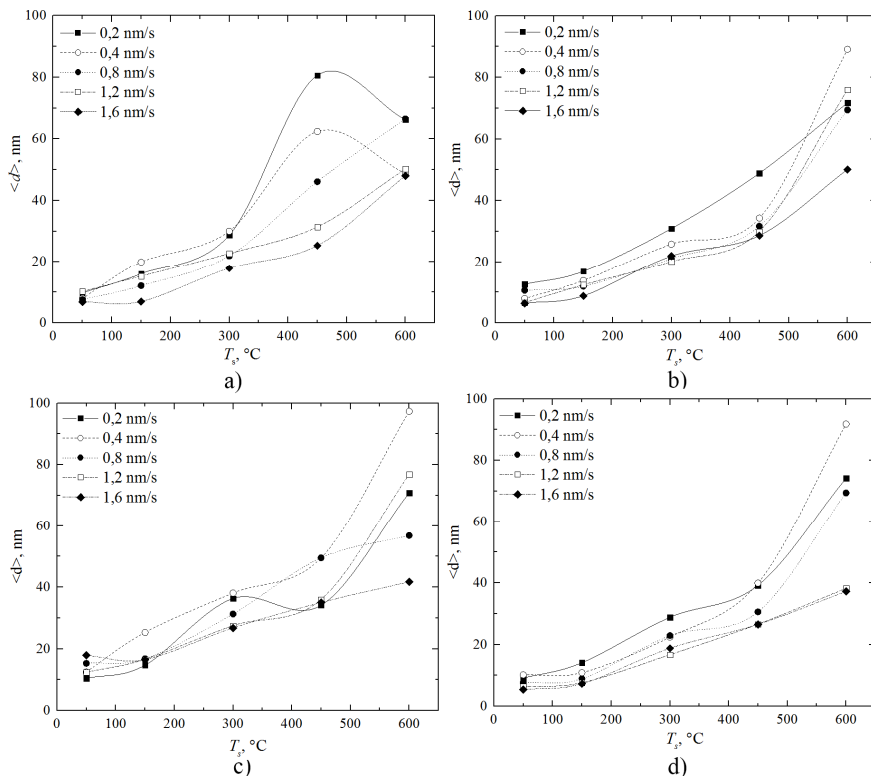


**Fig. 2.8** Crystallite size dependence on the substrate temperature of SDC thin films deposited by evaporating powders of different specific surface area on SiO<sub>2</sub> substrates: a)  $S_{BET} = 6.2 \text{ m}^2/\text{g}^{[D2]}$ , b)  $S_{BET} = 11.3 \text{ m}^2/\text{g}$ , c)  $S_{BET} = 38.82 \text{ m}^2/\text{g}^{[D1]}$ , d)  $S_{BET} = 201.3 \text{ m}^2/\text{g}$

## 2.4. Investigation of Surface Morphology of SDC Thin Films

SDC thin films deposited on 50 °C substrates have cracks, see **Fig. 2.9**. In addition, the number of cracks is higher when using a higher deposition rate during the deposition process, as shown in **Fig. 2.9, a, b, c, d, e**. Moreover, the existence of cracks depends on the substrate type. SDC thin films deposited on SiO<sub>2</sub>, Si(100), and Al<sub>2</sub>O<sub>3</sub> substrates produce cracks when using any of the deposition rates. However, SDC thin films deposited on Alloy600 substrates develop cracks only when employing the 1.6 nm/s deposition rate and the 50 °C temperature substrate, as demonstrated in **Fig. 2.9, f**. The influence of the substrate type is more

visible when using 150 °C temperature substrates. SDC thin films deposited on SiO<sub>2</sub> and Al<sub>2</sub>O<sub>3</sub> substrates exhibit cracks when using 1.2 nm/s and 1.6 nm/s deposition rates, see **Fig. 2.9, g, h**. SDC thin films deposited on Si(100) substrates develop cracks only when using the 1.6 nm/s deposition rate, as shown in **Fig. 2.9, i**; SDC thin films deposited on Alloy600 substrates are without cracks.

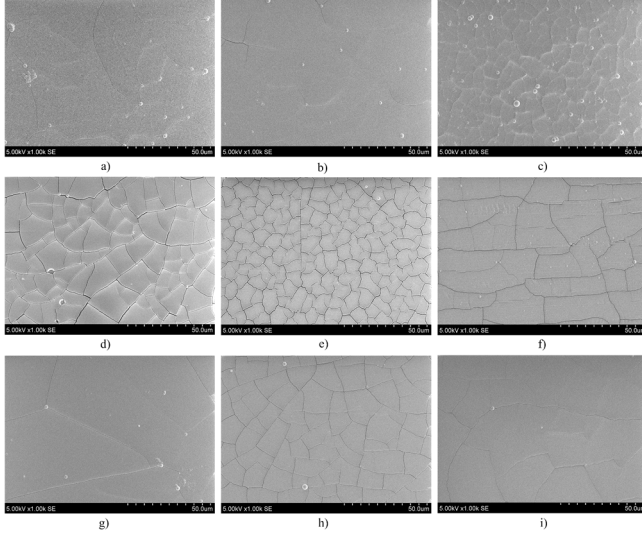


**Fig. 2.9** Topographic photos of SDC thin films deposited when evaporating powder of 201.3 m<sup>2</sup>/g specific surface area: a)  $v_g=0.2$  nm/s,  $T_s=50$  °C, SiO<sub>2</sub> substrate, b)  $v_g=0.4$  nm/s,  $T_s=50$  °C, SiO<sub>2</sub> substrate, c)  $v_g=0.8$  nm/s,  $T_s=50$  °C, SiO<sub>2</sub> substrate, d)  $v_g=1.2$  nm/s,  $T_s=50$  °C, SiO<sub>2</sub> substrate, e)  $v_g=1.6$  nm/s,  $T_s=50$  °C, SiO<sub>2</sub> substrate, f)  $v_g=1.6$  nm/s,  $T_s=50$  °C, Alloy600 substrate, g)  $v_g=1.2$  nm/s,  $T_s=150$  °C, SiO<sub>2</sub> substrate, h)  $v_g=1.6$  nm/s,  $T_s=150$  °C, SiO<sub>2</sub> substrate, and i)  $v_g=1.6$  nm/s,  $T_s=150$  °C, Si(100) substrate

Cracks are formed during island coalescence. Sudden coalescence of islands occurs when islands approach each other at certain distance  $d$ , i.e., the atoms on the side of an island move from their equilibrium positions towards the grain boundary[57-59]. Tensile stresses appear due to such reorganization of the structure. Moreover, the magnitude of tensile stresses depends on the surface diffusion speed. The higher is the surface diffusion speed, the smaller cracks are formed. Atoms are capable to migrate longer distances and reduce tensile stresses if the surface diffusion is fast, i.e., at high temperatures (300 °C–600 °C) and low deposition rates (0.2 nm/s–0.8 nm/s). It means that at these temperatures and deposition rates, no cracks should develop.

The influence of the substrate type can be explained by the fact that different substrates are denoted by different surface energies and different thermal expansion coefficients. It is possible that Alloy600 substrates have a higher surface



energy than other substrates. This is the cause of the interaction between the substrate and the island getting stronger. Islands must be closer to each other so that coalescence could occur. For this reason, the shift of atoms at an island's side is shorter. Therefore, tensile stresses are lower.

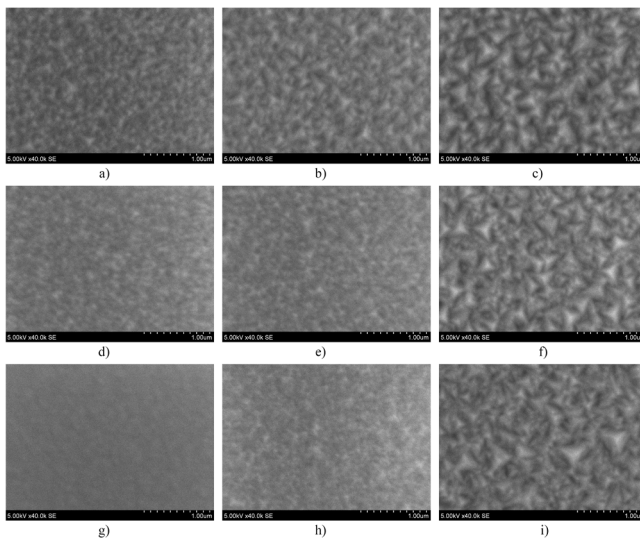


**Fig. 2.10** Topographic photos of SDC thin films deposited by evaporating powder of  $11.3 \text{ m}^2/\text{g}$  specific surface area on  $\text{SiO}_2$  substrates: a)  $T_s=50 \text{ }^\circ\text{C}$ ,  $v_g=0.2 \text{ nm/s}$ , b)  $T_s=150 \text{ }^\circ\text{C}$ ,  $v_g=0.2 \text{ nm/s}$ , c)  $T_s=300 \text{ }^\circ\text{C}$ ,  $v_g=0.2 \text{ nm/s}$ , d)  $T_s=50 \text{ }^\circ\text{C}$ ,  $v_g=0.8 \text{ nm/s}$ , e)  $T_s=150 \text{ }^\circ\text{C}$ ,  $v_g=0.8 \text{ nm/s}$ , f)  $T_s=300 \text{ }^\circ\text{C}$ ,  $v_g=0.8 \text{ nm/s}$ , g)  $T_s=50 \text{ }^\circ\text{C}$ ,  $v_g=1.6 \text{ nm/s}$ , h)  $T_s=150 \text{ }^\circ\text{C}$ ,  $v_g=1.6 \text{ nm/s}$ , i)  $T_s=300 \text{ }^\circ\text{C}$ ,  $v_g=1.6 \text{ nm/s}$

The deposition rate and the substrate temperature influence the grain size, shape, and arrangement, as shown in **Fig. 2.10** and **Fig. 2.11**. The diffusion length is longer when using substrates of a higher temperature whereas the number of grains is greater when using a higher deposition rate. It means that larger grains are formed when using higher temperature substrates and a lower deposition rate, see **Fig. 2.10**.

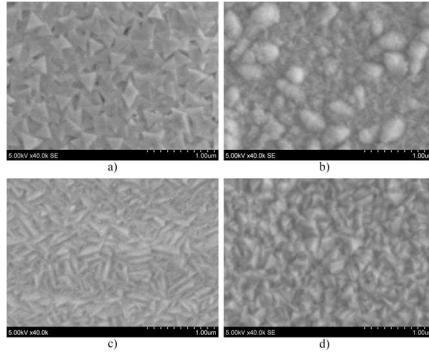


**Fig. 2.11** Topographic photos of SDC thin films with different preferential crystallographic orientation: a)  $v_g=1.6$  nm/s,  $T_s=600$  °C, SiO<sub>2</sub> substrate,  $S_{BET}=201.3$  m<sup>2</sup>/g, (111) orientation, b)  $v_g=1.6$ ,  $T_s=600$  °C, Si(100) substrate,  $S_{BET}=6.2$  m<sup>2</sup>/g, (200) orientation, c) Alloy600 substrate,  $v_g=0.2$ ,  $T_s=450$  °C,  $S_{BET}=6.2$  m<sup>2</sup>/g, (220) orientation<sup>[D2]</sup>, d) Alloy600 substrate,  $v_g=1.2$ ,  $T_s=600$  °C,  $S_{BET}=11.3$  m<sup>2</sup>/g, (311) orientation

In addition, SDC thin films have a different surface morphology when using different deposition parameters. However, changes in the microstructure occur only when using high temperature substrates and high deposition rates, as shown in **Fig. 2.11**. Mansila and Laukaitis obtained comparable results[54, 60]. The growth of thin films is coincident with the changes of the texture coefficient. Surface images of SDC thin films with different preferred orientation are presented in **Fig. 2.11**: **Fig. 2.11, a** – (111) orientation, **Fig. 2.11, b** – (200) orientation, **Fig. 2.11, c** – (220) orientation, and **Fig. 2.11, d** – (311) orientation.

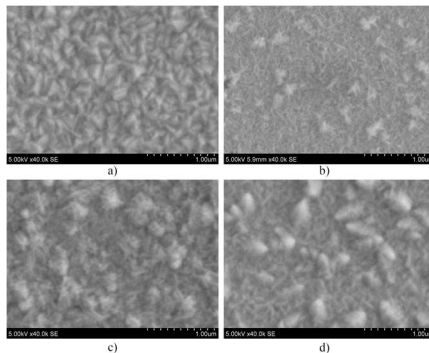


**Fig. 2.12** Topographic photos of SDC thin films of (311) crystallographic orientation: a) Alloy600,  $v_g=1.2$  nm/s,  $T_s=600$  °C, 11.3 m<sup>2</sup>/g, b) SiO<sub>2</sub>,  $v_g=1.6$  nm/s,  $T_s=600$  °C, 38.8 m<sup>2</sup>/g<sup>[D1]</sup>, c) Alloy600,  $v_g=0.8$  nm/s,  $T_s=600$  °C, 11.3 m<sup>2</sup>/g, d) Alloy600,  $v_g=0.4$  nm/s,  $T_s=600$  °C, 11.3 m<sup>2</sup>/g

However, grains form larger clusters with an increasing number of crystallographic orientations and their texture coefficients, as shown in **Fig. 2.12** and **Table 2.1**. **Fig. 2.12, a** demonstrates that the preferred orientation is (311). Moreover, this SDC thin film contains (111), (200), (220) crystallographic orientations as well. Nevertheless, the texture coefficients of these orientations are much smaller in comparison to (311) orientation, as shown in **Table 2.1**. SDC thin films grow with (111), (200), (220), (311), (222), and (400) crystallographic orientations in **Fig. 2.12, d**, where the texture coefficients of additional orientations, as shown in **Table 2.1**, are similar to the texture coefficient of the preferred orientation.

**Table 2.1** Texture coefficients of SDC thin films

$v_g$ , nm/s	$T_s$ , °C	Substrate	$S_{BET}$ , m <sup>2</sup> /g	$T_{(hkl)}$					
				<111>	<200>	<220>	<311>	<222>	<400>
1.2	600	SiO <sub>2</sub>	11.3	0.2	0.3	0.2	3.2	-	-
1.6	600	SiO <sub>2</sub>	38.8	0.6	1.6	0.1	2.3	0.3	-
0.8	600	Alloy600	11.3	0.3	1.0	0.7	2.3	-	0.8
0.4	600	Alloy600	11.3	0.6	1.0	0.9	2.5	0.4	0.7

SDC thin films grow according to the structure zone models of Movchan-Demchishin and Grovenor in Zone I and Zone T, see **Fig. 2.13**, **Fig. 2.14**[61, 62]. SDC thin films grow by forming small grains when using low temperature substrates (50 °C–150 °C), see **Fig. 2.13, a, b**. The grain size increases with the increasing temperature. Grains start growing on top of each other thus forming columns when 300 °C temperature substrates are used, as shown in **Fig. 2.13, c**. The columnar structure is more visible at higher temperatures, as shown in **Fig. 2.14, a**.

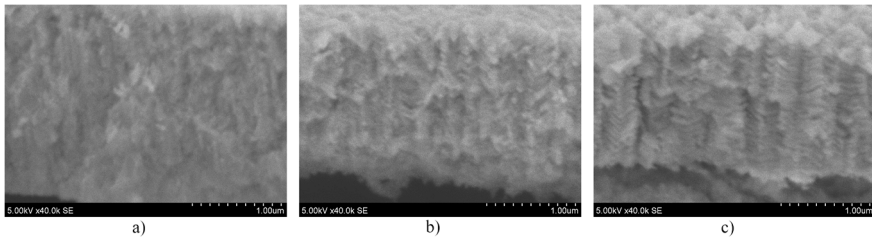


**Fig. 2.13** Cross-section photos of SDC thin films deposited by evaporating powder of 11.3 m<sup>2</sup>/g specific surface area on Alloy600 substrates while using 0.8 nm/s deposition rate: a)  $T_s=50$  °C, b)  $T_s=150$  °C, c)  $T_s=300$  °C

The type of SDC thin films growth depends on the preferred orientation at high substrate temperatures, as shown in **Fig. 2.14**. The grains grow on top of each other thus forming columns if the preferred crystallographic orientation is (111). The columns are formed of oblong grains if the preferred orientation is (200), (220) or (311).

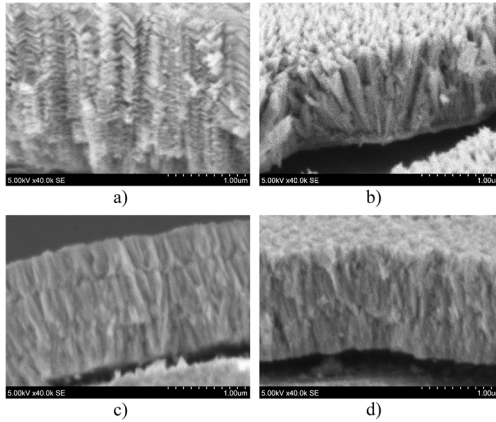


**Fig. 2.14** Cross section photos of SDC thin films deposited on Alloy600 substrates: a)  $v_g=0.2$  nm/s,  $T_s=600$  °C,  $11.3$  m<sup>2</sup>/g (111), b)  $v_g=1.6$  nm/s,  $T_s=450$  °C,  $6.2$  m<sup>2</sup>/g (200), c)  $v_g=0.2$  nm/s,  $T_s=450$  °C,  $6.2$  m<sup>2</sup>/g (220), d)  $v_g=1.2$  nm/s,  $T_s=600$  °C,  $11.3$  m<sup>2</sup>/g (311)

Density calculations prove that SDC thin films grow in Zone 1 and Zone T. Thin films growing in Zone 1 and Zone T feature low density due to a high number of grain boundaries and a high number of nanopores[61, 62]. The density of SDC thin films is  $\sim 3.50$  g/cm<sup>3</sup> (the theoretical density is  $7.15$  g/cm<sup>3</sup>) when using low temperatures ( $150$  °C– $300$  °C). In addition, microcracks exert influence on the density of thin films. The density of SDC thin films is higher when using substrates of a higher temperature. It reaches  $6.18$  g/cm<sup>3</sup> when using substrates of  $600$  °C. The deposition rate influences the density of thin films as well. The higher number of pores, grains and grain boundaries form when using a higher deposition rate. Consequently, SDC thin films have a lower density when using a higher deposition rate.

## 2.5. Investigation of the Surface Roughness of SDC Thin Films

Calculations of the surface roughness of SDC thin films deposited on SiO<sub>2</sub> substrates showed that it varies from  $2.2$  nm to  $50.8$  nm depending on the deposition parameters. The surface roughness decreases ( $\langle R_q \rangle$ , a decrease from  $20.0$  nm to  $8.0$  nm is observed) if powders of a higher specific surface area ( $S_{BET}$ ,  $6.2$  m<sup>2</sup>/g,  $11.3$  m<sup>2</sup>/g, and  $38.8$  m<sup>2</sup>/g) are evaporated, see **Fig. 2.15**. However, the roughness of SDC thin films increases ( $\langle R_q \rangle = 25.7$  nm) when the powder of  $201.3$  m<sup>2</sup>/g specific surface area is evaporated. The same pattern of variation is observed when drawing the dependence function of the minimum and maximum values of roughness on  $S_{BET}$  powder, see **Figure 2.15**.

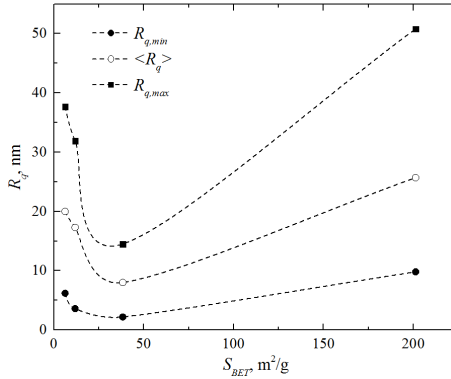


**Fig. 2.15** Dependence of SDC thin film surface roughness ( $R_q$ ) on the specific surface area  $S_{BET}$  of the evaporating powder, where  $R_{q,min}$  are the lowest surface roughness values using a certain  $S_{BET}$  powder,  $R_{q,max}$  is the highest surface roughness values obtained when using a particular  $S_{BET}$  powder, whereas  $\langle R_q \rangle$  represents average surface roughness values obtained when using a specific  $S_{BET}$  powder.

The dependence of the surface roughness of SDC thin films on the substrate temperature is non-linear. The surface roughness is higher when using higher temperature substrates, i.e., when the substrate temperature is 50 °C–300 °C, as shown in **Fig. 2.16, a**. However, the surface roughness of SDC thin films is lower when using a higher substrate temperature, that is, when the temperature of the substrate is 300 °C–600 °C. The temperature of 300 °C is the limiting temperature. The growth rate also determines the resulting surface roughness. The surface roughness of SDC thin films is lower by maintaining a higher deposition rate of SDC thin films. However, such a change is noticeable only at low substrate temperatures, as shown in **Fig. 2.16, b**, when evaporating the powder of 201.3 m<sup>2</sup>/g. This is due to the fact that the sizes of islands are smaller at high deposition rates, whereas the jumps of CeO and CeO<sub>2</sub> from the top of the islands to the substrate are more frequent. Similar results were obtained by Galdikas *et al.* and by Virbukas[41, 63]. The surface roughness of SDC thin films increases at high temperatures (450 °C–600 °C) with the increasing deposition rate of 0.8 nm/s–1.2 nm/s. It is possible that the dissociation of CeO and CeO<sub>2</sub> takes place at high substrate temperatures. For this reason, the speed of jumps of atoms from the top of the island is lower. Thus thin films grow more chaotically. When SDC thin films are formed by evaporating smaller surface area powder, the surface roughness values are more scattered: for example, 6.2 m<sup>2</sup>/g, as shown in **Fig. 2.16, c, d** or 201.3 m<sup>2</sup>/g, as seen in **Fig. 2.16, a, b**. This is especially noticeable when comparing the dependences of the surface roughness on the deposition rate, cf.

**Fig. 2.16, b, d.** Changes in the preferred (111) orientation and the appearance of other crystallographic planes ((200), (220), (311) and (400)) as well as their number could influence such a variation of surface roughness.

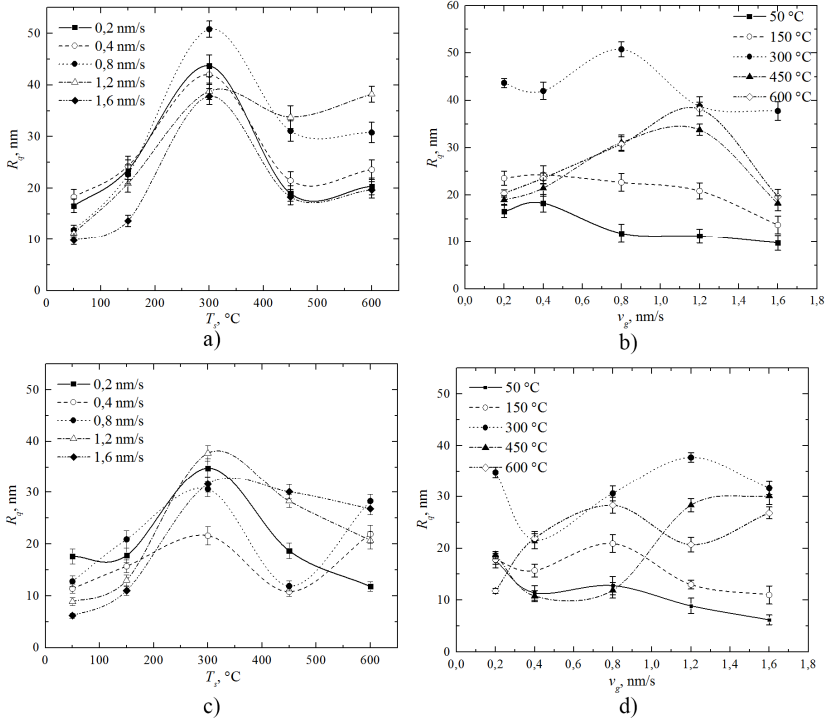


**Fig. 2.16** Dependence of SDC thin film surface roughness  $R_q$  on the temperature of the substrate ( $\text{SiO}_2$ ) ( $T_s$ ) and the deposition rate of thin films ( $v_j$ ): a) and b)  $S_{BET} = 201.3 \text{ m}^2/\text{g}$ , c) and d)  $S_{BET} = 6.2 \text{ m}^2/\text{g}$

Moreover, it is known that the surface roughness increases with the increasing crystallite size[64]. The  $Rq=f(\langle d \rangle)$  plot for SDC thin films which were deposited on  $\text{SiO}_2$  substrates by evaporating powder of the  $201.3 \text{ m}^2/\text{g}$  specific surface area yields information that the surface roughness increases with the increasing crystallite size, as demonstrated in **Fig. 2.17**. However, the surface roughness only increases until crystallites have reached  $\sim 25 \text{ nm}$  size. Subsequently, the surface roughness decreases with the increasing crystallite size. Thus there is another factor affecting the surface roughness variation. According to J. Zhang, the surface roughness of Cu thin films is lower when using substrates of higher temperatures because the adatom diffusion speed and length increases

with the increasing substrate temperature[65]. In a more detailed way, the dependence of surface roughness on the adatom diffusion length is described by Galdikas[66]. The dependence of the surface roughness on the temperature and the crystallite size can be explained on the grounds of his theory.

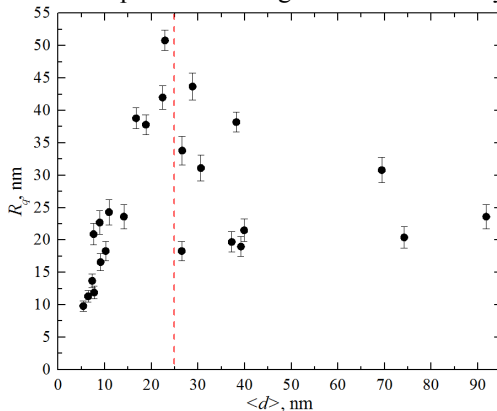


**Fig. 2.17** Dependence of surface roughness ( $R_q$ ) on the crystallite size ( $\langle d \rangle$ ) of SDC thin films deposited on  $\text{SiO}_2$  substrates by evaporating powder of  $201.3 \text{ m}^2/\text{g}$  specific surface area

It is possible to calculate the crystallite dimension only in one direction when using the XRD method, i.e., transversely to thin film. For this reason, it is assumed that crystallites are spheres, and that their dimensions transversely and along the thin film should be the same. In real life situations, these dimensions are different.

The speed and length of surface diffusion of adatoms are small when using low temperature substrates during deposition. It means that adatoms stay on the surface of islands, adatoms do not jump from the surface of the islands on the substrate. Thus crystallites grow faster vertically than horizontally. Crystallites grow larger when using a higher temperature. Therefore, the surface roughness is also higher. However, the surface diffusion speed increases with the increasing substrate temperature; meanwhile, the ratio of transverse dimensions to longitudinal dimensions decreases. Finally, when the surface diffusion length is larger than the longitudinal dimensions of crystallite ( $\sim 25 \text{ nm}$ ), adatoms jump from the surface of islands on the surface of the substrate. For this reason, the surface roughness is smaller when using high substrate temperatures during deposition. This was proven by AFM investigation, as shown in **Fig. 2.18**. The crystallite size is  $18.8 \text{ nm}$ – $26.5 \text{ nm}$  according to XRD calculations. Similar grain sizes are observed in AFM images, as seen in **Fig. 2.18, a**, when the temperature is  $50 \text{ }^\circ\text{C}$ . However, longitudinal dimensions increase by about  $200 \text{ nm}$  when using  $300 \text{ }^\circ\text{C}$ – $450 \text{ }^\circ\text{C}$  temperature substrates during deposition, as shown in **Fig. 2.18**,

**b, c.** In addition, the density of thin films is higher when using higher temperature substrates. Denser films contain fewer pores, which, of course, results in a smoother surface.

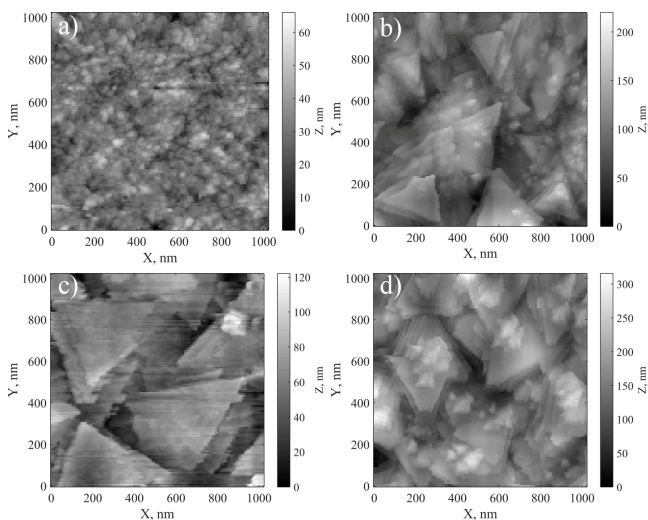


**Fig. 2.18** AFM images of SDC thin films deposited on SiO<sub>2</sub> substrates by evaporating powder of 201.3 m<sup>2</sup>/g specific surface area when using 1.6 nm/s deposition rate and different substrate temperature: a) 50 °C, b) 300 °C, c) 450 °C, and d) 600 °C

## 2.6. Evaluation of the Band Gap Energy of SDC Thin Films

SDC thin films are transparent to visible light which is proven by optical transmittance measurements. Optical transmittance of SDC thin films reaches about 80%. In order to evaluate the influence of dopant concentration on the optical band gap, calculations were carried out for SDC thin films containing crystallites of a similar size (22.0 nm±1.0 nm). It is thus possible to disregard the influence of the crystallite size on the optical band gap. Calculations prove the statement that the optical band gap depends on the dopant concentration. The optical band gap of SDC thin films decreases from 3.40 eV to 3.37 eV with Sm concentration increasing from 6.3 mol% to 12.0 mol%, as shown in **Fig. 2.19**.



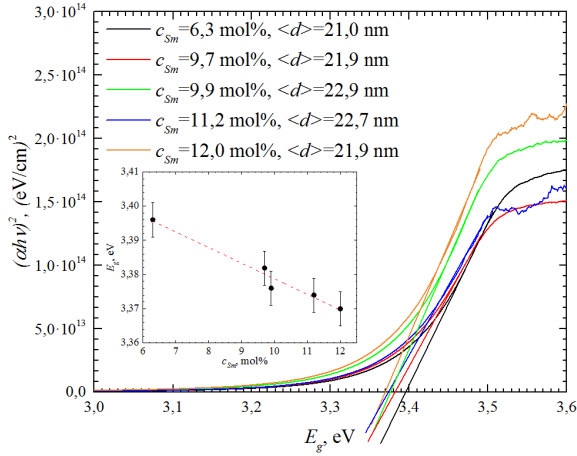


**Fig. 2.19**  $(h\nu\alpha)^2$  dependence on the photon energy and band gap ( $E_g$ ) dependence on the dopant concentration ( $c_{Sm}$ )

In order to evaluate the influence of the crystallite size on the optical band gap, calculations were carried out for SDC thin films with a similar dopant concentration ( $10.6 \text{ mol}\% \pm 1.5 \text{ mol}\%$ ). It was discovered that the optical band gap increases with the increasing crystallite size as it is evident from **Fig. 2.20**. The acceptor levels are formed above the valence levels when Ce is doped by Sm. For this reason, the energy of the electron jump is smaller as shown in **Fig. 2.21**.

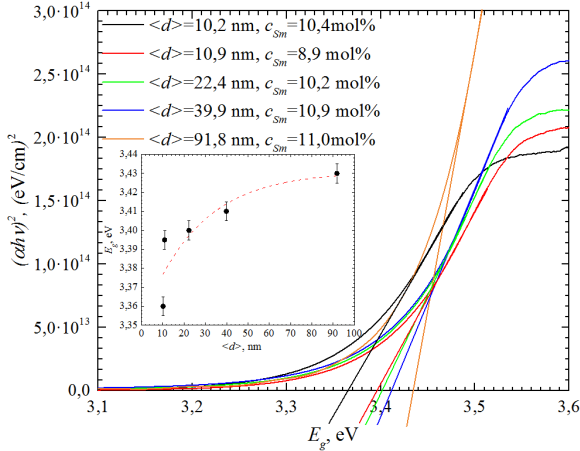


**Fig. 2.20**  $(h\nu\alpha)^2$  dependence on the photon energy and band gap ( $E_g$ ) dependence on the crystallite size ( $\langle d \rangle$ )

The number of oxygen vacancies increases with the decreasing crystallite size because the surface area increases where reduction occurs[67]. The concentration of  $Ce^{3+}$  increases with the increasing concentration of oxygen vacancies. For this reason, the donor level of  $Ce^{3+}$  forms beneath the conduction band. It means that the width of the band gap decreases.

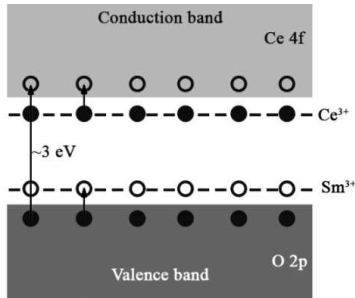


**Fig. 2.21** Electron energy levels for Sm-doped nanocrystalline ceria thin films[68, 69]

Calculations of the optical band gap for other thin films did not reveal any dependences on the crystallite size and Sm concentration. The optical band gap varies within the interval of 3.29 eV–3.74 eV due to the joint influence of the crystallite size, the Sm concentration, and the preferential crystallographic orientation.

## 2.7. Investigation of the Electrical Properties of SDC Thin Films

The measurements of impedance (thin films on  $Al_2O_3$  substrates) and the calculations of ionic conductivity revealed that the total conductivity of SDC thin films varies from  $3.4 \cdot 10^{-8}$  S/cm to 0.011 S/cm. The given values of ionic conductivity are calculated for the impedance results measured at a temperature of 600 °C. The highest value of total conductivity is similar to the value obtained by other authors: 15SCD–0.013 S/cm. In addition, the total conductivity of SDC thin films is lower than that of  $Bi_2V_{1.9}Cu_{0.1}O_{5.535}$  (0.33 S/cm) and  $La_{0.85}Sr_{0.15}Ga_{0.2}Mg_{0.2}O_{2.825}$  (0.0301 S/cm), but higher than 8YSZ (0.0064 S/cm),  $La_{1.8}Gd_{0.2}Mo_2O_9$  (0.0071 S/cm),  $La_{9.75}Sr_{0.25}Si_6O_{26.875}$  (0.010 S/cm)[13-15, 18-21, 70-97]. Such high ionic conductivity is influenced by the crystallite size, the grain shape, the crystallite orientation, the dopant concentration, and the  $Ce^{3+}$  concentration.

Ceria becomes conductive for oxygen ions when oxygen vacancies ( $2[V_O^{\bullet}] \approx [RE'_{Ce}]$ ) are created by doping it with lower valence dopants (Sm, Gd)[23]. It is also known that ceria loses oxygen with the decreasing partial pressure of oxygen and the increasing substrate temperature. It means that the reduction of  $Ce^{4+}$  to  $Ce^{3+}$  occurs, i.e., oxygen vacancies and electrons  $2[V_O^{\bullet}] \approx [e']$  are created[24-27].

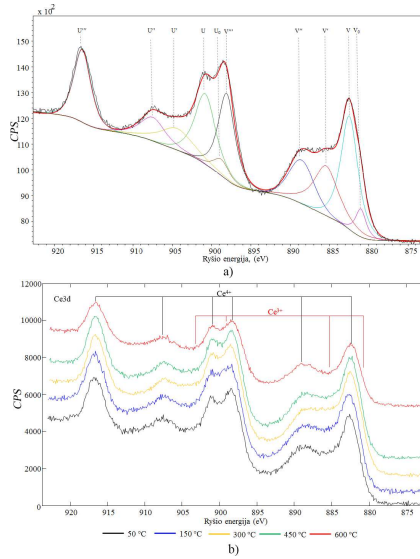


**Fig. 2.22** XPS spectra of Ce 3d spin orbit doublet of SDC thin films deposited by evaporating powder of 6.2 m<sup>2</sup>/g specific surface area on Al<sub>2</sub>O<sub>3</sub> substrates: a)  $T_s=300$  °C and  $v_g=0.2$  nm/s [ $V_0 - \text{Ce}^{3+}3d_{5/2}$ ,  $V - \text{Ce}^{4+}3d_{5/2}$ ,  $V' - \text{Ce}^{3+}3d_{3/2}$ ,  $V'' - \text{Ce}^{4+}3d_{3/2}$ ,  $V''' - \text{Ce}^{4+}3d_{5/2}$ ,  $U_0 - \text{Ce}^{3+}3d_{3/2}$ ,  $U - \text{Ce}^{4+}3d_{3/2}$ ,  $U' - \text{Ce}^{3+}3d_{5/2}$ ,  $U'' - \text{Ce}^{4+}3d_{5/2}$ ,  $U''' - \text{Ce}^{4+}3d_{3/2}$ ], and b)  $v_g=0.2$  nm/s<sup>[D2]</sup>

XPS measurements of SDC thin films deposited by evaporating powder of 6.2 m<sup>2</sup>/g specific surface area on Al<sub>2</sub>O<sub>3</sub> substrates proves the hypothesis about the reduction of Ce<sup>4+</sup> to Ce<sup>3+</sup>, see **Fig. 2.22, a, Table 2.2**<sup>[D2]</sup>. The concentration of Ce<sup>3+</sup> varies from 24.5% to 29.1%. However, no relationship between Ce<sup>3+</sup> and conductivity was observed as shown in **Table 2.2**. It is reasonable to consider that electrical conductivity changes due to the component of ionic conductivity because the change of Ce<sup>3+</sup> concentration is in the range of 5%. However, the concentration of Ce<sup>3+</sup> is high whereas the mobility of electrons is higher than the mobility of oxygen ions. Therefore, the component of electronic conductivity should be high and possibly higher than the component of ionic conductivity. However, it is not possible to separate the components of the ionic and electronic conductors by using two Pt electrode configuration in EIS measurements. Ionic conductivity and electronic conductivity components could be distinguished from one another by using electrodes blocking electronic or ionic conductivity or by calculating the oxygen diffusion coefficient by using conduction relaxation plots<sup>[98, 99]</sup>. The above listed methods require special equipment and expensive materials. For example, gold is used to form electrodes blocking ionic conductivity<sup>[99]</sup>. For these reasons, notation of total conductivity will be used

without any separation between components of ionic conductivity versus electronic conductivity.

**Table 2.2** Total conductivity and  $Ce^{3+}$  concentration in SDC thin films deposited by evaporating powder of  $6.2 \text{ m}^2/\text{g}$  specific surface area on  $\text{Al}_2\text{O}_3$  substrates by using  $0.2 \text{ nm/s}$  deposition rate<sup>[D2]</sup>

$\sigma$ , S/cm	$2.7 \cdot 10^{-3}$	$2.1 \cdot 10^{-4}$	$1.2 \cdot 10^{-3}$	$1.1 \cdot 10^{-2}$	$4.2 \cdot 10^{-3}$
$C_{Ce^{3+}}$ , %	25.6	24.5	29.1	26.8	28.1

The activation energy of oxygen vacancies changes from  $0.770 \text{ eV}$  to  $1.042 \text{ eV}$ . No relationship was observed between the total conductivity and the activation energy of oxygen vacancies. Thus it is possible to think that the microstructure and growth kinetics exerts the most prominent influence on the total conductivity. However, it is still necessary to evaluate the influence of the dopant concentration on the total conductivity of SDC thin films. The total conductivity increases with the increasing concentration of Sm in thin films as shown in **Fig. 2.23**. Therefore, in order to evaluate the influence of the microstructure, SDC thin films with similar Sm concentration will be compared.

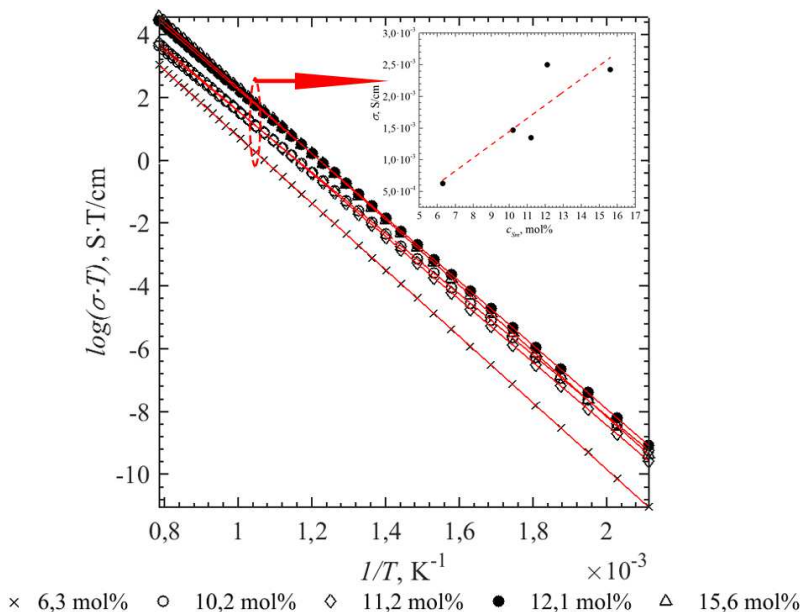


**Fig. 2.23** Arrhenius plots of SDC thin films with different dopant concentrations

Nyquist plots of SDC thin films feature two semicircles corresponding to the impedances of grain and grain boundaries. Hence a fitting procedure was carried out by using a circuit of  $R_g|Q_g-R_{gr}|Q_{gr}$ . The quality of the fitting procedure

was controlled by using  $Z_{re}=f(\log(\omega))$  and  $-Z_{im}=f(\log(\omega))$  plots as shown in **Fig. 2.25**. The fitted curves must match the experimental ones in all the plots.

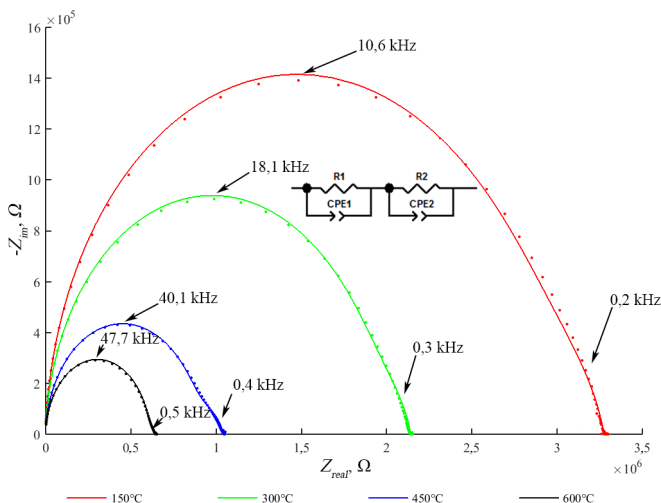


**Fig. 2.24** Nyquist plots of SDC thin films deposited by evaporating powder of 203.3 m<sup>2</sup>/g specific surface area when using 0.4 nm/s deposition rate

The semicircle of grain boundaries is smaller than the grain semicircle as seen in **Fig. 2.24**. The Nyquist plot obtains this type of shape due to the influence of the crystallite size. The ionic conductivity decreases while the electronic conductivity increases with the decreasing crystallite size. The increased ratio between the grain boundary width ( $2b$ ) and the grain width ( $L$ ) is the reason of the decrease in ionic conductivity because grain boundaries exert a blocking effect on the diffusion of oxygen ions[100]. The grain boundaries which are parallel to the migration path of oxygen ions (i.e., which are perpendicular to the electrodes) influence the ionic conductivity[31, 101]. However, it is not possible to decompose the measured impedance of the grain into impedances of the grain boundary and the grain itself because it is not possible to separate impedances of components connected in parallel in an equivalent circuit[102]. For these reasons, it is considered that the semicircle in a high frequency range corresponds to the ‘grain’ conductivity. However, the influence of the grain boundaries increases to ionic and electronic conductivities with the decreasing grain size. Therefore, a semicircle of ‘grains’ covers the semicircle of grain boundaries (the grain boundaries are positioned perpendicular to the migration path of oxygen ions).

That is why, only  $R_g + R_{gb}$  resistivity is visible in  $Z_{re}=f(\log(\omega))$  plots as shown in **Fig. 2.25, a**”. It decreases (from 3.28 M $\Omega$  to 0.65 M $\Omega$ ) in SDC thin films which were deposited on higher temperature substrates.  $R_g + R_{gb}$  resistivity was decomposed into its components after the fitting procedure exhibited in **Table 2.3**.

It was revealed that the resistivity of ‘grains’ ( $R_g$ ) is about 10 times higher than the resistivity of grain boundaries ( $R_{gr}$ ).

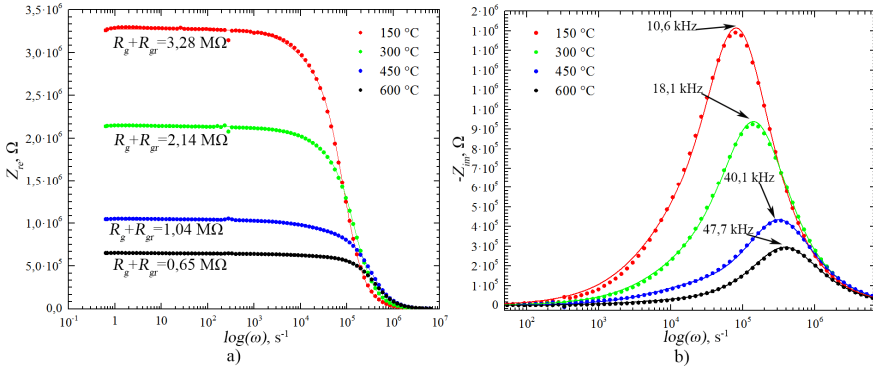


**Fig. 2.25** a)  $Z_{re}$  dependences on  $\log(\omega)$  and b)  $-Z_{im}$  dependences on  $\log(\omega)$  for SDC thin films deposited by evaporating powder of  $203.3\text{m}^2/\text{g}$  specific surface area while using  $0.4\text{ nm/s}$  deposition rate

Only one peak corresponding to the relaxation frequency is visible in  $-Z_{im}=f(\log(\omega))$  plot although there should be two peaks, see **Fig. 2.25, b**. The relaxation frequency increases from 10.6 kHz to 47.7 kHz in SDC thin films which were deposited on higher temperature substrates. However, the two relaxation frequencies were extracted from  $-Z_{im}=f(\log(\omega))$  plot after conducting the fitting procedure. The results demonstrated that the relaxation frequency of oxygen ions in ‘grains’ is 10 times higher than in the grain boundaries whereas the relaxation time is 100 times shorter in ‘grains’ ( $\tau_g$ ) than in the grain boundaries ( $\tau_{gr}$ ) as shown in **Table 2.3**. It follows that the total conductivity should increase when using higher temperature substrates during the deposition of SDC thin films. In addition, it was observed that accurate analysis of EIS measurements is possible only after conducting the fitting procedure.

**Table 2.3** Fitting parameters of Nyquist plots ( $R$  stands for resistivity,  $Q$  represents the capacitance of the constant phase element,  $\alpha$  denotes a constant), critical frequency ( $f_c$ ), and relaxation time ( $\tau$ )

$v_g$ , nm/s	$T_s$ , K	$R_g$ , $\Omega$	$R_{gr}$ , $\Omega$	$Q_g$ , F	$Q_{gr}$ , F	$\alpha_g$	$\alpha_{gr}$	$f_{cg}$ , Hz	$\tau_g$ , s	$f_{cgr}$ , Hz	$\tau_{gr}$ , s
0.4	50	$9.80 \cdot 10^8$	$5.06 \cdot 10^7$	$5.60 \cdot 10^{-11}$	$1.86 \cdot 10^{-9}$	0.69	0.70	$2.90 \cdot 10^0$	$5.49 \cdot 10^{-2}$	$1.69 \cdot 10^0$	$9.41 \cdot 10^{-2}$
	150	$2.77 \cdot 10^6$	$5.05 \cdot 10^5$	$5.40 \cdot 10^{-12}$	$1.33 \cdot 10^{-9}$	0.98	0.80	$1.06 \cdot 10^4$	$1.50 \cdot 10^{-5}$	$2.37 \cdot 10^2$	$6.72 \cdot 10^{-4}$
	300	$1.86 \cdot 10^6$	$2.82 \cdot 10^5$	$4.72 \cdot 10^{-12}$	$1.70 \cdot 10^{-9}$	0.98	0.80	$1.81 \cdot 10^4$	$8.78 \cdot 10^{-6}$	$3.32 \cdot 10^2$	$4.79 \cdot 10^{-4}$
	450	$8.66 \cdot 10^5$	$1.76 \cdot 10^5$	$4.58 \cdot 10^{-12}$	$2.35 \cdot 10^{-9}$	0.98	0.80	$4.01 \cdot 10^4$	$3.97 \cdot 10^{-6}$	$3.85 \cdot 10^2$	$4.14 \cdot 10^{-4}$
	600	$6.02 \cdot 10^5$	$4.49 \cdot 10^4$	$5.54 \cdot 10^{-12}$	$1.04 \cdot 10^{-8}$	0.98	0.80	$4.77 \cdot 10^4$	$3.34 \cdot 10^{-6}$	$3.41 \cdot 10^2$	$4.67 \cdot 10^{-4}$

The quantitative calculations of the total conductivity prove that (**Fig. 2.26**). For example, the total conductivities of SDC thin films deposited by evaporating powder of the 201.3 m<sup>2</sup>/g specific surface area on Al<sub>2</sub>O<sub>3</sub> substrates while using 0.4 nm/s deposition rate are  $4.4 \cdot 10^{-7}$  S/cm,  $9.0 \cdot 10^{-4}$  S/cm,  $1.5 \cdot 10^{-3}$  S/cm,  $3.3 \cdot 10^{-3}$  S/cm, and  $7.3 \cdot 10^{-3}$  S/cm if, respectively, 50 °C, 150 °C, 300 °C, 450 °C, and 600 °C temperature substrates are used. The values of the total conductivity are calculated for experimental points measured at a temperature of 500 °C. The total conductivity is higher when using substrates of a higher temperature during deposition as shown in **Fig. 2.26**. In addition, SDC thin films deposited on 50 °C temperature substrates exhibit a much lower total conductivity.

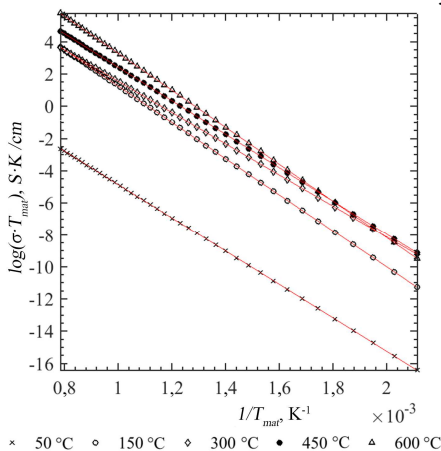


**Fig. 2.26** Arrhenius plot of SDC thin films deposited by evaporating powder of 201.3m<sup>2</sup>/g specific surface area while using 0.4 nm/s deposition rate

The total conductivity is also influenced by the deposition rate of SDC thin films as seen in **Fig. 2.27**. For example, the total conductivities are  $2.6 \cdot 10^{-3}$  S/cm,  $1.5 \cdot 10^{-3}$  S/cm,  $8.2 \cdot 10^{-4}$  S/cm,  $5.8 \cdot 10^{-6}$  S/cm, and  $8.4 \cdot 10^{-6}$  S/cm for SDC thin films which are deposited by evaporating powder of  $6.2 \text{ m}^2/\text{g}$  specific surface area on  $150 \text{ }^\circ\text{C}$  temperature  $\text{Al}_2\text{O}_3$  substrates (the dopant concentration of  $\sim 11.1 \text{ mol}\%$ , **Table 2.4**) while using  $0.2 \text{ nm/s}$ ,  $0.4 \text{ nm/s}$ ,  $0.8 \text{ nm/s}$ ,  $1.2 \text{ nm/s}$ , and  $1.6 \text{ nm/s}$  deposition rate

**Table 2.4**  $S_m$  concentration ( $c_{Sm}$ ) and its standard deviations ( $S_n$ ) in SDC thin films deposited by evaporating powder of  $6.2 \text{ m}^2/\text{g}$  specific surface area on  $600 \text{ }^\circ\text{C}$  temperature substrates ( $T_s$ ) while using various deposition rates ( $v_g$ )

$T_s, \text{ }^\circ\text{C}$	$v_g = 0.2 \text{ nm/s}$		$v_g = 0.4 \text{ nm/s}$		$v_g = 0.8 \text{ nm/s}$		$v_g = 1.2 \text{ nm/s}$		$v_g = 1.6 \text{ nm/s}$	
	$c_{Sm}, \text{ mol}\%$	$S_n, \text{ mol}\%$	$c_{Sm}, \text{ mol}\%$	$S_n, \text{ mol}\%$	$c_{Sm}, \text{ mol}\%$	$S_n, \text{ mol}\%$	$c_{Sm}, \text{ mol}\%$	$S_n, \text{ mol}\%$	$c_{Sm}, \text{ mol}\%$	$S_n, \text{ mol}\%$
150	11.1	0.4	12.5	0.4	10.3	1.4	11.4	1.2	10.1	2.0

This implies that the total conductivity of SDC thin films is lower when using a higher deposition rate. In addition, thin films exhibit extremely low total conductivity if they are deposited while using  $1.2 \text{ nm/s}$  and  $1.6 \text{ nm/s}$  deposition rates as shown in **Fig. 2.27**.

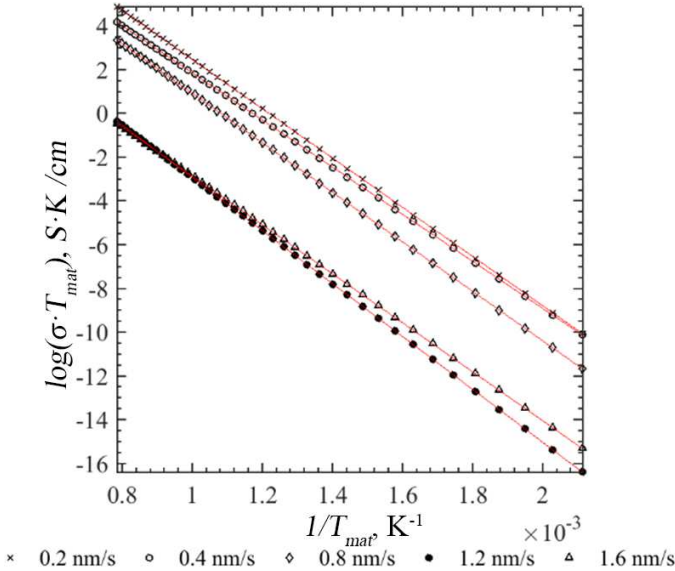


**Fig. 2.27** Arrhenius plot of SDC thin films deposited by evaporating powder of  $6.2 \text{ m}^2/\text{g}$  specific surface area on  $150 \text{ }^\circ\text{C}$  temperature substrates <sup>[D2]</sup>



The influence of deposition parameters on the total conductivity is related with changes in microstructure. Thin films feature cracks if they are deposited on low temperature (50 °C–150 °C) substrates while using a high deposition rate (1.2 nm/s–1.6 nm/s), see **Fig. 2.3**. Therefore, these thin films are denoted by extremely low total conductivity ( $3.4 \cdot 10^{-8}$  S/cm– $3.9 \cdot 10^{-6}$  S/cm). In addition, the variation of the crystallite size is in good agreement with the variation of the total conductivity, see **Fig. 2.28**. The total conductivity is lower than 0.002 S/cm if the crystallite size is about 10 nm–25 nm and more than 0.006 S/cm if the crystallite size is bigger than 90 nm.

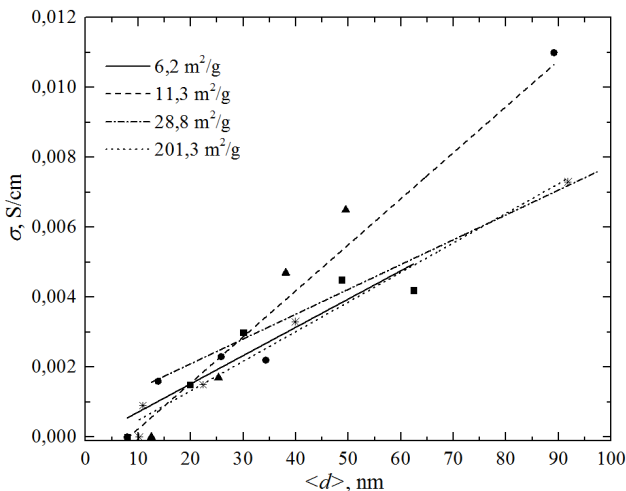


**Fig. 2.28** Dependence of the total conductivity ( $\sigma$ ) on the crystallite size ( $\langle d \rangle$ )

## CONCLUSIONS

1. The required power of the e-beam for maintaining the same deposition speed decreases by 1.5 times (from 485 W to 301 W) when powder of 201.3 m<sup>2</sup>/g specific surface area instead of powder of 6.2 m<sup>2</sup>/g specific surface area is used because atoms on the surface of the particles have a lower binding energy than the atoms inside the particles.
2. The preferential crystallographic orientation (111) changes to (200), (220), (311) or (222) if the 450 °C–600 °C substrate temperature and 1.2 nm/s–1.6 nm/s deposition rate are used during deposition. The process is the most prominent for SDC thin films deposited on Alloy600 substrates and the weakest for SDC thin films deposited on SiO<sub>2</sub> substrates.
3. The preferential crystallographic orientation (111) tends to change its orientation to (200), (220) or (311) by evaporating the powder of 6.2 m<sup>2</sup>/g specific surface area, to (220) or (311) by evaporating powders of 11.3 m<sup>2</sup>/g and 38.8 m<sup>2</sup>/g specific surface areas, and to (311) or (222) by evaporating the powder of 201.3 m<sup>2</sup>/g specific surface area. Moreover, a lower number of SDC thin films change the preferential crystallographic orientation.
4. The crystallite size changes from 5.4 nm to 149.3 nm. The crystallite size increases by about 8 times by changing the substrate temperature from 50 °C to 600 °C and by about 2 times by changing the deposition rate from 0.2 nm/s to 1.2 nm/s.
5. SDC thin films deposited on 150 °C temperature SiO<sub>2</sub>, Si(100), and Al<sub>2</sub>O<sub>3</sub> substrates are homogeneous if 0.2 nm/s–0.8 nm/s deposition rate is used, and SDC thin films deposited on Alloy600 substrates are homogeneous if 0.2 nm/s–1.6 nm/s deposition rate is used. SDC thin films deposited on 300 °C–600 °C temperature SiO<sub>2</sub>, Si(100), Al<sub>2</sub>O<sub>3</sub> and Alloy600 substrates are homogeneous when 0.2 nm/s–1.6 nm/s deposition rate is used.
6. Triangular grains grow on top of each other and form columns when the temperature of 50 °C to 300 °C is used during deposition. Triangular grains lose their shape, whereas longitudinal grains grow when using high temperature substrates (450 °C and 600 °C) and high deposition rates (1.2 nm/s and 1.6 nm/s) due to the change of the preferential crystallographic orientation from (111) to (200), (220), (311) or (222).
7. The surface roughness changes depending on the longitudinal and transverse dimensions of grains. The surface roughness increases when the crystallite sizes are smaller than 25 nm. When crystallites are larger than 25 nm, the surface roughness decreases due to the different growth rates of grains in the parallel and perpendicular directions to the substrate.
8. The band gap increases from 3.36 eV to 3.43 eV with the crystallite size increasing from 10.2 nm to 91.8 nm.
9. The total conductivity increases with the increasing crystallite size. The values of total conductivity are about 2.0·10<sup>-3</sup> S/cm when the crystallite size is 10.0 nm–25.0 nm and 6.0·10<sup>-3</sup> S/cm when the crystallite size is 80.0 nm. The highest value of the total conductivity is 1.1·10<sup>-2</sup> S/cm when the crystallite sizes are 80.6 nm and 89.1 nm.

## List of References

1. AHMED, O. *Future Building Gas Sensing Applications*, in *Solid State Gas Sensors - Industrial Application*. 2012, Springer-Verlag Berlin Heidelberg. 3-12.
2. HARYANTO, A., et al. Current Status of Hydrogen Production Techniques by Steam Reforming of Ethanol: A Review. *Energy & Fuels*. 2005, 19(5), 2098-2106.
3. BOUDGHENE STAMBOULI, A. and E. TRAVERSA. Fuel cells, an alternative to standard sources of energy. *Renewable and Sustainable Energy Reviews*. 2002, 6(3), 295-304.
4. RAMAMOORTHY, R., et al. Oxygen sensors: Materials, methods, designs and applications. *Journal of Materials Science*. 2003, 38(21), 4271-4282.
5. GARZON, F., et al. Dense diffusion barrier limiting current oxygen sensors. *Sensors and Actuators B: Chemical*. 1998, 50(2), 125-130.
6. MËNIL, F., et al. Critical review of nitrogen monoxide sensors for exhaust gases of lean burn engines. *Sensors and Actuators B: Chemical*. 2000, 67(1-2), 1-23.
7. SHIMAMOTO, Y., et al. Performance and stability of potentiometric CO<sub>2</sub> gas sensor based on the Pt, Li<sub>2</sub>CO<sub>3</sub>/Na<sub>2</sub>O–Al<sub>2</sub>O<sub>3</sub>–4SiO<sub>2</sub>/YSZ/Pt electrochemical cell. *Sensors and Actuators B: Chemical*. 2004, 99(1), 113-117.
8. PASIERB, P. and M. REKAS. Solid-state potentiometric gas sensors—current status and future trends. *Journal of Solid State Electrochemistry*. 2009, 13(1), 3-25.
9. BASTUCK, M., et al. A new approach to self-monitoring of amperometric oxygen sensors. *Sensors and Actuators B: Chemical*. 2015, 214, 218-224.
10. HUIJSMANS, J. P. P., et al. Intermediate temperature SOFC – a promise for the 21st century. *Journal of Power Sources*. 1998, 71(1-2), 107-110.
11. GE, B., et al. Sr<sub>2</sub>FeNbO<sub>6</sub> Applied in Solid Oxide Electrolysis Cell as the Hydrogen Electrode: Kinetic Studies by Comparison with Ni-YSZ. *Electrochimica Acta*. 2015, 151, 437-446.
12. BASU, R. N. *Materials for Solid Oxide Fuel Cells*, in *Recent Trends in Fuel Cell Science and Technology*. 2007, Springer New York: New York, NY. 286-331.
13. KHARTON, V. V., et al. Transport properties of solid oxide electrolyte ceramics: a brief review. *Solid State Ionics*. 2004, 174(1-4), 135-149.
14. SKINNER, S. J. and J. A. KILNER. Oxygen ion conductors. *Materials Today*. 2003, 6(3), 30-37.
15. SAMMES, N. M., et al. Bismuth based oxide electrolytes— structure and ionic conductivity. *Journal of the European Ceramic Society*. 1999, 19(10), 1801-1826.
16. SCHRÖDER, F., et al. Temperature dependence of Bi<sub>2</sub>O<sub>3</sub> structural parameters close to the  $\alpha$ - $\delta$  phase transition. *Phase Transitions*. 2010, 83(5), 311-325.
17. BEVILACQUA, M., et al. Preparation, Characterization, and Electrochemical Properties of Pure and Composite LaNi<sub>0.6</sub>Fe<sub>0.4</sub>O<sub>3</sub>-Based Cathodes for IT-SOFC. *Chemistry of Materials*. 2007, 19(24), 5926-5936.

18. GUO, X., et al. Ionic conduction in zirconia films of nanometer thickness. *Acta Materialia*. 2005, 53(19), 5161-5166.
19. DANIELE, P., et al. Probing the bulk ionic conductivity by thin film hetero-epitaxial engineering. *Science and Technology of Advanced Materials*. 2015, 16(1), 015001.
20. YANG, S. M., et al. Strongly enhanced oxygen ion transport through samarium-doped CeO<sub>2</sub> nanopillars in nanocomposite films. *Nature Communications*. 2015, 6, 8588.
21. ACHARYA, S. A., et al. Gd/Sm dopant-modified oxidation state and defect generation in nano-ceria. *Solid State Ionics*. 2014, 260, 21-29.
22. FUENTES, R. O. and R. T. BAKER. Synthesis and properties of Gadolinium-doped ceria solid solutions for IT-SOFC electrolytes. *International Journal of Hydrogen Energy*. 2008, 33(13), 3480-3484.
23. TULLER, H. L. and S. R. BISHOP. Point Defects in Oxides: Tailoring Materials Through Defect Engineering. *Annual Review of Materials Research*. 2011, 41(1), 369-398.
24. MIGANI, A., et al. Greatly facilitated oxygen vacancy formation in ceria nanocrystallites. *Chemical Communications*. 2010, 46(32), 5936-5938.
25. WANG, H.-F., et al. A Model to Understand the Oxygen Vacancy Formation in Zr-Doped CeO<sub>2</sub>: Electrostatic Interaction and Structural Relaxation. *The Journal of Physical Chemistry C*. 2009, 113(23), 10229-10232.
26. KATO, S., et al. Quantitative depth profiling of Ce<sup>3+</sup> in Pt/CeO<sub>2</sub> by in situ high-energy XPS in a hydrogen atmosphere. *Physical Chemistry Chemical Physics*. 2015, 17(7), 5078-5083.
27. HAYLES, J. and H. BAO. The reduction and oxidation of ceria: A natural abundance triple oxygen isotope perspective. *Geochimica et Cosmochimica Acta*. 2015, 159, 220-230.
28. GOBEL, M. C., et al. Numerical calculations of space charge layer effects in nanocrystalline ceria. Part I: comparison with the analytical models and derivation of improved analytical solutions. *Physical Chemistry Chemical Physics*. 2014, 16(21), 10214-10231.
29. KIM, S., et al. Space charge conduction: Simple analytical solutions for ionic and mixed conductors and application to nanocrystalline ceria. *Physical Chemistry Chemical Physics*. 2003, 5(11), 2268-2273.
30. GOBEL, M. C., et al. Numerical calculations of space charge layer effects in nanocrystalline ceria. Part II: detailed analysis of the space charge layer properties. *Physical Chemistry Chemical Physics*. 2014, 16(21), 10175-10186.
31. GOBEL, M. C., et al. Mixed conductivity in nanocrystalline highly acceptor doped cerium oxide thin films under oxidizing conditions. *Physical Chemistry Chemical Physics*. 2011, 13(23), 10940-10945.
32. TSCHÖPE, A. Grain size-dependent electrical conductivity of polycrystalline cerium oxide II: Space charge model. *Solid State Ionics*. 2001, 139(3-4), 267-280.
33. VIRBUKAS, D. and G. LAUKAITIS. The structural and electrical properties of samarium doped ceria films formed by e-beam deposition technique. *Solid State Ionics*. 2017, 302, 107-112.

34. LAUKAITIS, G. and D. VIRBUKAS. The structural and electrical properties of GDC10 thin films formed by e-beam technique. *Solid State Ionics*. 2013, 247, 41-47.
35. VIRBUKAS, D. *Cerio oksido elektrolitų formavimas garinant elektronų spinduliu*. In *Fizikos katedra*. 2011, Kauno technologijos universitetas: Kaunas.
36. BAIL, A. L. *Chapter 5 The Profile of a Bragg Reflection for Extracting Intensities*, in *Powder Diffraction: Theory and Practice*. 2008, The Royal Society of Chemistry. 134-165.
37. NAGARAJU, P., et al. Optical and microstructural studies on laser ablated nanocrystalline CeO<sub>2</sub> thin films. *Glass Physics and Chemistry*. 2015, 41(5), 484-488.
38. DUDONIS, J. *Plonų dangų fizika ir nanotechnologijos*. 2007: Šiaulių universiteto leidykla. 226.
39. NANDA, K. K., et al. Liquid-drop model for the size-dependent melting of low-dimensional systems. *Physical Review A*. 2002, 66(1), 013208.
40. NANDA, K. K. Size-dependent melting of nanoparticles: Hundred years of thermodynamic model. *Pramana*. 2009, 72(4), 617-628.
41. GALDIKAS, A., et al. Real-time kinetic modeling of YSZ thin film roughness deposited by e-beam evaporation technique. *Applied Surface Science*. 2008, 255(5), 1929-1933.
42. WATANABE, K., et al. *Method for vapor depositing a cerium oxide film*. 1980, Google Patents.
43. Phelly Materials. *Cerium Oxide*. 2017. [žiūrėta 2017-04-23]. Prieiga per: <http://www.phelly.com/cerium-oxide/>.
44. CHAVAN, S. V., et al. Phase Relations and Thermal Expansion Studies in the Ceria–Yttria System. *Journal of the American Ceramic Society*. 2004, 87(10), 1977-1980.
45. BARNA, P. B. and M. ADAMIK. Fundamental structure forming phenomena of polycrystalline films and the structure zone models. *Thin Solid Films*. 1998, 317(1–2), 27-33.
46. SARAIVA, M. *Sputter Deposition of MgO Thin Films: The Effect of Cation Substitution In Faculteit Wetenschappen* 2012, Universiteit Gent Gent.
47. SIMKOVICH, G. *Transport in Nonstoichiometric Compounds*. 2012: Springer.
48. CHINARRO, E., et al. Bulk and grain boundary conductivity of Ca<sub>0.97</sub>Ti<sub>1-x</sub>FexO<sub>3-δ</sub> materials. *Solid State Ionics*. 2003, 160(1), 161-168.
49. BULFIN, B., et al. Analytical Model of CeO<sub>2</sub> Oxidation and Reduction. *The Journal of Physical Chemistry C*. 2013, 117(46), 24129-24137.
50. CHONG GEOL, K., et al. Growth of Si Thin Films on CeO<sub>2</sub> /Si(111) Substrate Using Electron-Beam Evaporation. *Japanese Journal of Applied Physics*. 2001, 40(8R), 4769.
51. CHIKYOW, T., et al. Reaction and regrowth control of CeO<sub>2</sub> on Si(111) surface for the silicon-on-insulator structure. *Applied Physics Letters*. 1994, 65(8), 1030.
52. NARASIMHA RAO, K., et al. Studies on single layer CeO<sub>2</sub> and SiO<sub>2</sub> films deposited by rotating crucible electron beam evaporation. *Materials Science and Engineering: B*. 2003, 98(1), 38-44.

53. ANWAR, M. S., et al. Study of nanocrystalline ceria thin films deposited by e-beam technique. *Current Applied Physics*. 2011, 11(1, Supplement), S301-S304.
54. MANSILLA, C. Structure, microstructure and optical properties of cerium oxide thin films prepared by electron beam evaporation assisted with ion beams. *Solid State Sciences*. 2009, 11(8), 1456-1464.
55. PIACENTE, V., et al. Dissociation energy of CeO<sub>2</sub> and Ce<sub>2</sub>O<sub>3</sub> molecules. *The Journal of Chemical Physics*. 1973, 59(1), 31-36.
56. ORLIUKAS, A. F., et al. XPS and impedance spectroscopy of some oxygen vacancy conducting solid electrolyte ceramics. *Solid State Ionics*. 2011, 188(1), 36-40.
57. NIX, W. D. and B. M. CLEMENS. Crystallite coalescence: A mechanism for intrinsic tensile stresses in thin films. *Journal of Materials Research*. 2011, 14(8), 3467-3473.
58. FREUND, L. B. and E. CHASON. Model for stress generated upon contact of neighboring islands on the surface of a substrate. *Journal of Applied Physics*. 2001, 89(9), 4866-4873.
59. GOH, G. K. L., et al. Cracking of low temperature solution deposited CeO<sub>2</sub> thin films. *Journal of Electroceramics*. 2006, 16(4), 575-579.
60. LAUKAITIS, G., et al. Gadolinium doped ceria thin films deposited by e-beam technique. *Solid State Ionics*. 2008, 179(1), 66-71.
61. MOVCHAN, B. A. Study of the Structure and Properties of Thick Vacuum Condensates of Nickel, Titanium, Tungsten, Aluminium Oxide and Zirconium Oxide. *Fiz Met Metalloved*. 1969, 28.
62. GROVENOR, C. R. M., et al. The development of grain structure during growth of metallic films. *Acta Metallurgica*. 1984, 32(5), 773-781.
63. VIRBUKAS, D. and G. LAUKAITIS. The structural and electrical properties of samarium doped ceria films formed by e-beam deposition technique. *Solid State Ionics*. 2017, 302(Supplement C), 107-112.
64. ZHANG, X., et al. Thickness dependence of grain size and surface roughness for dc magnetron sputtered Au films. *Chinese Physics B*. 2010, 19(8), 086802.
65. ZHANG, J., et al. Comparison of Cu thin films deposited on Si substrates with different surfaces and temperatures. *Applied Surface Science*. 2013, 276, 417-423.
66. GALDIKAS, A. Non-monotonous dependence of surface roughness on factors influencing energy of adatoms during thin island film growth. *Surface Science*. 2006, 600(13), 2705-2710.
67. DUTTA, P., et al. Concentration of Ce<sup>3+</sup> and Oxygen Vacancies in Cerium Oxide Nanoparticles. *Chemistry of Materials*. 2006, 18(21), 5144-5146.
68. AMANO, F., et al. Effect of Ti<sup>3+</sup> Ions and Conduction Band Electrons on Photocatalytic and Photoelectrochemical Activity of Rutile Titania for Water Oxidation. *The Journal of Physical Chemistry C*. 2016, 120(12), 6467-6474.
69. BHARTI, B., et al. Formation of oxygen vacancies and Ti(3+) state in TiO<sub>2</sub> thin film and enhanced optical properties by air plasma treatment. *Scientific Reports*. 2016, 6, 32355.
70. MAHATO, N., et al. Doped zirconia and ceria-based electrolytes for solid oxide fuel cells: a review. *Nanomaterials and Energy*. 2012, 1(1), 27-45.

71. VALOV, I., et al. Ionic and electronic conductivity of nitrogen-doped YSZ single crystals. *Solid State Ionics*. 2009, 180(28–31), 1463-1470.
72. JIANG, J., et al. Improved ionic conductivity in strained yttria-stabilized zirconia thin films. *Applied Physics Letters*. 2013, 102(14), 143901.
73. PETERS, A., et al. Ionic conductivity and activation energy for oxygen ion transport in superlattices — The multilayer system CSZ (ZrO<sub>2</sub> + CaO) / Al<sub>2</sub>O<sub>3</sub>. *Solid State Ionics*. 2007, 178(1–2), 67-76.
74. YAO, L., et al. Enhanced conductivity of (110)-textured ScSZ films tuned by an amorphous alumina interlayer. *Physical Chemistry Chemical Physics*. 2015, 17(35), 23034-23040.
75. PIVA, R. H., et al. Improving physical properties of cubic InO<sub>1.5</sub>-stabilized zirconia by alloying with MoO<sub>3</sub>. *Journal of Alloys and Compounds*. 2016, 685, 593-603.
76. ANITHAKUMARI, P., et al. Utilizing non-stoichiometry in Nd<sub>2</sub>Zr<sub>2</sub>O<sub>7</sub> pyrochlore: exploring superior ionic conductors. *RSC Advances*. 2016, 6(100), 97566-97579.
77. WACHSMAN, E. D. and K. T. LEE. Lowering the Temperature of Solid Oxide Fuel Cells. *Science*. 2011, 334(6058), 935-939.
78. JUNG, D. W., et al. Effect of total dopant concentration and dopant ratio on conductivity of (DyO<sub>1.5</sub>)<sub>x</sub>–(WO<sub>3</sub>)<sub>y</sub>–(BiO<sub>1.5</sub>)<sub>1–x–y</sub>. *Acta Materialia*. 2010, 58(2), 355-363.
79. PEARCE, M. C. and V. THANGADURAI. Electrical transport properties of aliovalent cation-doped CeO<sub>2</sub>. *Asia-Pacific Journal of Chemical Engineering*. 2009, 4(1), 33-44.
80. LI, S., et al. Sinterability and electrical properties of ZnO-doped Ce<sub>0.8</sub>Y<sub>0.2</sub>O<sub>1.9</sub> electrolytes prepared by an EDTA–citrate complexing method. *Journal of Alloys and Compounds*. 2011, 509(1), 94-98.
81. KUHARUANGRONG, S. Ionic conductivity of Sm, Gd, Dy and Er-doped ceria. *Journal of Power Sources*. 2007, 171(2), 506-510.
82. FEI, Y., et al. Ionic Conductivities and Microstructures of Ytterbium-Doped Ceria. *Journal of the Electrochemical Society*. 2007, 154(2), B180-B185.
83. ABBASSI, M., et al. Ionic conductivity of apatite-type solid electrolyte ceramics Ca<sub>2–x</sub>Ba<sub>x</sub>La<sub>4</sub>Bi<sub>4</sub>(SiO<sub>4</sub>)<sub>6</sub>O<sub>2</sub> (0 ≤ x ≤ 2). *Ceramics International*. 2013, 39(8), 9215-9221.
84. ABRAM, E. J., et al. A novel enhancement of ionic conductivity in the cation-deficient apatite La<sub>9.33</sub>(SiO<sub>4</sub>)<sub>6</sub>O<sub>2</sub>. *Journal of Materials Chemistry*. 2001, 11(8), 1978-1979.
85. SOOD, K., et al. Structural, Conductivity, and Dielectric Relaxation Studies of La<sub>0.9</sub>Ba<sub>0.1</sub>GaO<sub>3–δ</sub> System. *Particulate Science and Technology*. 2015, 33(2), 113-118.
86. WEI, T., et al. Sr<sub>3–3x</sub>Na<sub>3x</sub>Si<sub>3</sub>O<sub>9–1.5x</sub> (x = 0.45) as a superior solid oxide-ion electrolyte for intermediate temperature-solid oxide fuel cells. *Energy & Environmental Science*. 2014, 7(5), 1680-1684.
87. STEVENSON, J. W., et al. Influence of Cobalt and Iron Additions on the Electrical and Thermal Properties of (La, Sr)(Ga, Mg)O<sub>3–δ</sub>. *Journal of the Electrochemical Society*. 2000, 147(9), 3213-3218.
88. NGUYEN, T. L., et al. The effect of oxygen vacancy on the oxide ion mobility in LaAlO<sub>3</sub>-based oxides. *Solid State Ionics*. 2000, 130(3–4), 229-241.

89. LYBYE, D. and N. BONANOS. Proton and oxide ion conductivity of doped LaScO<sub>3</sub>. *Solid State Ionics*. 1999, 125(1–4), 339-344.
90. SOOD, K., et al. Preferential occupancy of Ca<sup>2+</sup> dopant in La<sub>1-x</sub>Ca<sub>x</sub>InO<sub>3-δ</sub> (x = 0–0.20) perovskite: structural and electrical properties. *Ionics*. 2015, 21(10), 2839-2850.
91. HARIHARAN, R. and P. GOPALAN. Effect of A-site substitution on electrical conductivity and microstructure of YAlO<sub>3</sub>. *Journal of Materials Research*. 2012, 27(15), 2017-2023.
92. ISHIHARA, T., et al. Improved oxygen ion conductivity of NdAlO<sub>3</sub> perovskite-type oxide by doping with Ga. *Solid State Ionics*. 1994, 70, 234-238.
93. TSUJI, T., et al. Effect of ionic radius on electrical conductivity of doped SmAlO<sub>3</sub> perovskite oxide. *Solid State Ionics*. 2002, 154–155, 541-546.
94. XUEFENG, Z. and Y. WEISHEN. *Mixed Conducting Ceramic Membranes*. 1 ed. 2017, Springer-Verlag GmbH Germany: Springer-Verlag Berlin Heidelberg. XI, 367.
95. VERKERK, M. J. and A. J. BURGGRAAF. High Oxygen Ion Conduction in Sintered Oxides of the Bi<sub>2</sub>O<sub>3</sub>-Dy<sub>2</sub>O<sub>3</sub> System *Journal of the Electrochemical Society*. 1981, 128(1), 75-82.
96. TAKAHASHI, T., et al. High oxide ion conduction in the sintered oxides of the system Bi<sub>2</sub>O<sub>3</sub>-Gd<sub>2</sub>O<sub>3</sub>. *Journal of Applied Electrochemistry*. 1975, 5(3), 197-202.
97. BELOUSOV, V. V. Oxygen-permeable membrane materials based on solid or liquid Bi<sub>2</sub>O<sub>3</sub>. *MRS Communications*. 2013, 3(4), 225-233.
98. MAUVY, F., et al. Chemical oxygen diffusion coefficient measurement by conductivity relaxation—correlation between tracer diffusion coefficient and chemical diffusion coefficient. *Journal of the European Ceramic Society*. 2004, 24(6), 1265-1269.
99. BOUKAMP, B. A., et al. Ionic and electronic conductivity in lead–zirconate–titanate (PZT). *Solid State Ionics*. 2004, 170(3), 239-254.
100. CHIANG, Y. M., et al. Defect and transport properties of nanocrystalline CeO<sub>2-x</sub>. *Applied Physics Letters*. 1996, 69(2), 185-187.
101. KIM, S. and J. MAIER. On the Conductivity Mechanism of Nanocrystalline Ceria. *Journal of the Electrochemical Society*. 2002, 149(10), J73-J83.
102. MAIER, J. On the Conductivity of Polycrystalline Materials. *Berichte der Bunsengesellschaft für physikalische Chemie*. 1986, 90(1), 26-33.



## **A List of Scholarly Publications on the Topic of Dissertation**

**The Results Obtained in the Course of Doing this Research Have Been Published in the Following Journals Included into the Database of Web of Science Core Collection (*Clarivate Analytics*):**

1. [D1] SRIUBAS, M., LAUKAITIS, G. (2015). The Influence of the Technological Parameters on the Ionic Conductivity of Samarium Doped Ceria Thin Films. In: *Materials Science (Medžiagotyra)*, 2015, 21(1).
2. [D2] SRIUBAS, M., PAMAKŠTYS, K. and LAUKAITIS, G. (2017). Investigation of Microstructure and Electrical Properties of Sm Doped Ceria Thin Films. In: *Solid State Ionics*, 2017, 302, p. 165–172.
3. [D3] VIRBUKAS, D., SRIUBAS, M. and LAUKAITIS, G. (2015). Structural and Electrical Study of Samarium Doped Cerium Oxide Thin Films Prepared by E-Beam Evaporation. In: *Solid State Ionics*, 2015, 271, p. 98–102.
4. [D4] SRIUBAS, M., BOČKUTĖ, K., VIRBUKAS, D., and LAUKAITIS, G. (2015). Dynamics of Electrical Charge Carriers in Mg-Doped TiO<sub>2</sub> Thin Films under Reducing Conditions. In: *Journal of Vibroengineering*, 2015, 17(6).

**The Results Obtained in the Course of Doing this Research Have Been Published in the Following Peer-Reviewed Journals Included into the Database of Web of Science Core Collection (*Clarivate Analytics*):**

1. [D5] SRIUBAS, M., et al. (2014). Investigation of the Properties of Ca-Doped TiO<sub>2</sub> Thin Films Formed by E-Beam Evaporation. In: *Procedia Engineering*, 2014, 98, p. 133–138.

## SANTRAUKA

### SAMARIU LEGIRUOTO CERIO OKSIDO PLONŪJŲ SLUOKSNIŲ FORMAVIMAS IR TYRIMAS

Disertacijos tikslas – nustatyti garinamų miltelių savitojo paviršiaus ploto, augimo greičio, padėklo temperatūros ir padėklo rūšies įtaką plonųjų  $\text{Sm}_{0,2}\text{Ce}_{0,8}\text{O}_{2-\delta}$  sluoksnių, suformuotų garinant elektronų pluošteliu, savybėms. Mikrostruktūrinės, morfologinės, optinės ir elektrinės savybės ištirtos taikant XRD, SEM, EDS, XPS, UV-VIS, AFM ir EIS metodus.

Formuojant SDC dangas buvo pastebėta, kad elektronų pluoštelio galia, kurios reikia tam pačiam augimo greičiui palaikyti, yra mažesnė naudojant didesnio savitojo paviršiaus ploto miltelius. Pavyzdžiui, norint pasiekti 0,2 nm/s augimo greitį, kai naudojami 6,2 m<sup>2</sup>/g milteliai, reikia 485 W galios, o kai naudojami 201,3 m<sup>2</sup>/g milteliai – 301 W galios.

Atlikus XRD matavimus buvo nustatyta, kad vyraujanti (111) kristalografinė orientacija keičiasi esant aukštai temperatūrai (450–600 °C) ir palaikant didelį augimo greitį (1,2–1,6 nm/s). Ji keičiasi į (200), (220), (311) arba (222) orientaciją priklausomai nuo miltelių savitojo paviršiaus ploto. Be to, didėjant garinamų miltelių savitajam paviršiaus plotui vis mažiau sluoksnių keičia vyraujančią orientaciją. Dar daugiau, vyraujančią kristalografinę orientaciją labiausiai yra linkę keisti plonieji SDC sluoksniai, suformuoti ant Alloy600 padėklų, o mažiausiai – sluoksniai, suformuoti ant SiO<sub>2</sub> padėklų.

Nustatyta, kad suformuotuose SDC sluoksniuose kristalitų dydis kinta nuo 5,4 nm iki 149,3 nm. Keičiant naudojamą padėklų temperatūrą nuo 50 °C iki 600 °C kristalitų dydis išauga apie 8 kartus, o keičiant augimo greitį nuo 0,2 nm/s iki 1,6 nm/s kristalitų dydis sumažėja apie 2 kartus. Tačiau naudojant aukštos temperatūros (450–600 °C) padėklus kristalitų dydis gali sumažėti dėl vyraujančios orientacijos plokštumos pasikeitimo.

Nustatyta, kad kristalitų dydis daro įtaką paviršiaus šiurkštumui ir medžiagos elektrinėms bei optinėms savybėms. Paviršiaus šiurkštumas didėja augant kristalitų dydžiui. Tačiau kristalitų dydžiui viršijus ~25 nm paviršiaus šiurkštumas pradeda mažėti augant kristalitų dydžiui dėl skirtingo kristalitų augimo greičio statmenai padėklui ir lygiagrečiai su juo. Savitasis laidis taip pat kyla didėjant kristalitų dydžiui. Kristalitų dydžiui esant apie 10–25 nm savitasis laidis yra  $\sim 2 \cdot 10^{-3}$  S/cm, o kristalitų dydžiui esant daugiau nei 80 nm savitasis laidis viršija  $6 \cdot 10^{-3}$  S/cm. Didžiausias savitasis laidis yra  $1,1 \cdot 10^{-2}$  S/cm, kristalitų dydžiui esant 80,6 nm ir 89,1 nm. Be to, draustinės juostos plotis didėja nuo 3,36 eV iki 3,43 eV, kristalitų dydžiui augant nuo 10,2 nm iki 91,8 nm.

Naudojamą padėklų temperatūrą keičiant nuo 50 °C iki 300 °C, trikampaiai grūdėliai auga vienas ant kito sudarydami kolonas. Naudojant aukštą padėklų temperatūrą (450 °C ir 600 °C) ir didelį augimo greitį (1,2–1,6 nm/s), sluoksniai auga sudarydami kolonas iš pailgų grūdelių. Grūdėliai praranda trikampę formą dėl vyraujančios (111) orientacijos pasikeitimų.

## Curriculum Vitae

### Personal Information

Name, Surname: Mantas Sriubas  
Date of birth: August 31, 1988  
Place of birth: Anykščiai  
Nationality: Lithuanian  
Address: Kovo 11-osios 124-30, LT-49380, Kaunas, Lithuania  
E-mail: [mantas.sriubas@ktu.lt](mailto:mantas.sriubas@ktu.lt)

### Education

2013–2017 Kaunas University of Technology, Faculty of Mathematics and Natural Sciences, Department of Physics. *PhD studies*  
2011–2013 Kaunas University of Technology, Faculty of Mathematics and Natural Sciences. *Master's degree (with honor)*  
2007–2011 Mathematics and Natural Sciences. *Bachelor's degree*  
1995–2007 Anykščiai Antanas Vienuolis Gymnasium

### Work Experience

2017 Feb. – present Assistant at Kaunas University of Technology, Faculty of Mathematics and Natural Sciences, Department of Physics.  
2014 Sept. – 2016 Oct. Laboratory assistant at Kaunas University of Technology, Faculty of Mathematics and Natural Sciences, Department of Physics.  
2013 Nov. – 2014 Feb. Substitute teacher at Vytautas Magnus University *Rasa* Gymnasium  
2010 Sept. – 2011 Dec. Laboratory assistant at Lithuanian Energy Institute, Center for Hydrogen Technologies

### Additional Information

Seminars Science festivals 'Researchers' Night 2015', 'Spaceship Earth 2015'  
Seminar 'Young Scientists' ABC', 2011  
Member of organizing committee of the 12<sup>th</sup> International Symposium on Systems with Fast Ionic Transport, 2016  
Honors and Awards Doctoral scholarship 2014 for exceptional academic and scientific achievements.  
*Research Council of Lithuania* scholarship for 2016 for exceptional academic and scientific achievements.

UDK 546.655-31+539.234](043.3)

SL344. 2018-01-12, 3,25 leidyb. apsk. I. Tiražas 50 egz.

Išleido Kauno technologijos universitetas, K. Donelaičio g. 73, 44249 Kaunas  
Spausdino leidyklos „Technologija“ spaustuvė, Studentų g. 54, 51424 Kaunas